Research Square

Preprints are preliminary reports that have not undergone peer review.
They should not be considered conclusive, used to inform clinical practice,
or referenced by the media as validated information.

Symmetric and asymmetric vehicle models: coincidence of natural frequencies and the role of modal and interwheel correlations under random excitation

Gildas Amouzou

gildasamouzou2@gmail.com

Université Félix Houphouët-Boigny https://orcid.org/0009-0001-9439-0024

Émile Danho

Université Félix Houphouët-Boigny

Isaac Elishakoff

Florida Atlantic University https://orcid.org/0000-0002-1723-7771

Lassiné Kéita

Florida Atlantic University

Research Article

Keywords: Random vibration, Modal analysis, Repeated natural frequencies, Frequency coincidence, Vehicle dynamics, Interwheel correlations, RMS, Vibrational energy

Posted Date: November 10th, 2026

DOI: https://doi.org/10.21203/rs.3.rs-11667218/v1

License: This work is licensed under a Creative Commons Attribution 4.0 International License.
Read Full License

Additional Declarations: The authors declare no competing interests.

Symmetric and asymmetric vehicle models: coincidence of natural frequencies and the role of modal and interwheel correlations under random excitation

Gildas Yaovi Amouzou [(a)], Emile Danho [(a)], Isaac Elishakoff [(b)], Lassiné Kéita [(b,c)]

[(a)] Unité de Formation et de Recherche de Mathématique et Informatique, Laboratoire de Mécanique et Informatique, Université Félix Houphouët-Boigny.
[(b)] Department of Ocean and Mechanical Engineering, Florida Atlantic University, Boca Raton, FL 33431-0991, USA
[(c)] Centre de Recherche, Université de Bretagne Sud, Unité Mixte de Recherche CNRS 6027, Lorient, Cedex, France.

e-mail: gildasamouzou2@gmail.com; danhoemile@yahoo.com; elishako@fau.edu; lkeita2023@fau.edu
AGY, https://orcid.org/0009-0001-9439-0024
IE, https://orcid.org/0000-0002-1723-7771

Abstract

This study addresses the random vibration analysis of a seven-degree-of-freedom full vehicle model with repeated or closely spaced natural frequencies. It first revisits existing results: the literature has established that an ideal symmetric vehicle without anti-roll bars, with the origin of the reference frame at the center of the sprung mass, possesses four identical natural frequencies associated with the vertical displacements of the wheels. The study then generalizes these results by accounting for both the anti-roll bars and the height of the center of gravity. Closed-form expressions are derived for the critical heights at which two body frequencies coincide, in addition to the four identical wheel frequencies. For the symmetric vehicle, the heave-pitch frequency coincidence occurs at a critical height of 0.761 m, whatever the stiffness of the anti-roll bars. The heave-roll coincidence occurs at a critical height of 0.408 m without anti-roll bars and 1.280 m with them. For the asymmetric vehicle, by contrast, no coincidence is observed for the heave–pitch coupling; the roll frequency, however, coincides with a body mode at critical heights of 0.356 and 0.522 m without anti-roll bars, and 1.089 m with them. For the vibration analysis, two excitations are considered: a stationary white noise and a sinusoidal speed-bump profile, both applied to the four wheels with time delays determined by the wheelbase, the track and the vehicle speed. Two types of correlation are identified in the autocorrelation matrix of the generalized velocities: the modal cross-correlations and the correlations between the wheel excitations. Omitting the former, which produces the 75% error reported by Long et al. when a single wheel is excited, no longer matters when all four wheels are excited: the error remains below 0.16% under white noise and 0.8% under the speed bump, including at the critical heights. Omitting the latter, which amounts to assuming that the wheels are excited independently, leads instead to errors of 1,453 to 6,064% in roll and of several hundred percent in heave and pitch at low speeds. Such an omission removes both the left–right compensation and the interference between axles that govern the body response. The critical speed range of the vehicle lies between 5 and 30 km/h, where the delays between axles and between sides are equal to half a period of the pitch or roll vibration. Since the speed bump is a deterministic transient excitation, the RMS indicator is replaced by the vibrational energy. For an aspect ratio of 1/10, the body energy is maximal between 5 and 15 km/h, well below the 50 km/h threshold reported in the literature, whereas the wheel energy increases linearly with speed: maximum loading and maximum error therefore do not occur at the same speeds.

Keywords: Random vibration, Modal analysis, Repeated natural frequencies, Frequency coincidence, Vehicle dynamics, Interwheel correlations, RMS, Vibrational energy.

1. Introduction

The dynamic analysis of road vehicles has been a major concern for several decades, both for occupant safety and for ride comfort [1,2]. On a real road, the vehicle is permanently excited by pavement irregularities, which can only be described probabilistically [2,3]. Its response is therefore analyzed as that of a multi-degree-of-freedom mechanical system subjected to a random process, and the determination of its natural frequencies is the first step in characterizing the vibration modes associated with the motions of the body and the wheels. These frequencies are obtained from the eigenvalue problem of the system [4]. Beyond their mere identification, particular attention must be paid to possible frequency coincidences. Unlike a distinct natural frequency, which corresponds to a unique mode shape, a multiple frequency generates an eigenspace with no preferred basis: any linear combination of the associated eigenvectors remains admissible [4,5]. Lubliner and Elishakoff [6] showed that the non-uniqueness of the modal basis

does not affect the statistical quantities of the response, which are invariant under an orthogonal change of basis within the eigenspace, but that the modal cross-correlations become essential and can no longer be neglected. To our knowledge, this problem has been addressed for vehicles only by Long et al. [7] and by Elishakoff [5]. These authors established the existence of four identical frequencies for the running gear of an ideal symmetric vehicle without anti-roll bars, with the origin of the reference frame at the center of the sprung mass. They showed that the off-diagonal terms of the zero-lag autocorrelation matrix of the physical velocities are then no longer negligible. This matrix describes both the distribution of vibrational energy among the vehicle motions and the degree of coupling between these motions; omitting these terms distorts the representation of the overall behavior of the system.

The methodological framework for this type of spectral analysis is now classical. Established by Crandall and Mark [8] and later systematized by Lin [9] and Newland [10], it consists in deriving the spectral density matrix of the response from that of the excitation, the autocorrelation matrix then being obtained by inverse Fourier transform, generally evaluated by the residue method. On the excitation side, the description of the road profile as a stationary Gaussian process with a power-law spectral density dates back to Dodds and Robson [11] and underlies the ISO 8608 classification. Robson [12] explicitly introduced the cross-spectral density matrix of the multi-wheel excitation, accounting for the time lag between the four contact points; in the present work, this mechanism generates the interwheel delays, whose role proves decisive. More recently, Mikhlin et al. [13] studied a ten-degree-of-freedom vehicle model, which also exhibits pairs of very close natural frequencies, under harmonic, random and half-sine excitations, the latter representing the crossing of an obstacle. Their analysis, carried out by time-domain simulation, includes a delay between axles but assumes that the profiles on the two sides are uncorrelated. The consequences of this assumption for the vibration analysis of the vehicle, particularly for the roll response, are quantified precisely in the present work.

The work of Long et al. [7] nevertheless calls for a few remarks. The excitation is applied to a single wheel, with no delay between contact points, which is not representative of a moving vehicle and underestimates the transmitted energy by a factor of four. The error attributed to the omission of the modal cross-correlations is measured relative to the complete modal sum, obtained by the normal-mode method under the assumption of proportional damping, rather than relative to an exact solution independent of this assumption. The anti-roll bars and the height of the center of gravity, which modify the roll and pitch frequencies and hence the coincidences, are not taken into account. These authors do note, however, that for repeated frequencies the truncated response depends on the basis chosen in the eigenspace. This non-uniqueness is recovered in the present study at the critical heights of the center of gravity, a case not examined by the previous authors.

This paper deals with the random vibration analysis of a seven-degree-of-freedom full vehicle with coincident natural frequencies. Its first objective is to establish a complete analytical formulation of the seven natural frequencies of the model, including the stiffness and damping of the anti-roll bars, and to recover the results of the literature in the particular case where the origin of the reference frame is at the center of the sprung mass and the anti-roll bars are absent. The second objective is to derive closed-form expressions for the critical heights of the center of gravity at which two body frequencies of the symmetric vehicle coincide, with and without anti-roll bars. The heave-pitch frequency coincidence, which is independent of the presence of anti-roll bars, and the heave-roll frequency coincidence are both highlighted; in the latter configuration, the critical height increases with the bar stiffness. Finally, the third objective is to establish the correlation matrix of the generalized velocities for two distinct excitations, accounting for the four wheel–road contact points and their mutual delays, and to quantify both the error due to the omission of the modal cross-correlations and the error due to the omission of the correlations between the wheel excitations.

The paper is organized as follows. The equations of motion of the full model are first derived and then linearized under the assumption of small pitch and roll angles. The speed-bump profile and the interwheel delays are then modeled. The modal analysis is carried out for the symmetric and asymmetric configurations, and the frequency coincidences are discussed as functions of the height of the center of gravity and of the anti-roll bar stiffnesses. The autocorrelation matrix is computed by the residue method, unlike in Gao et al. [2], where it is evaluated by Monte Carlo simulation. The computation is first performed under stationary white noise and then for the crossing of a hump-type speed bump.

2. Equations of motion

The vehicle considered is a full model composed of a sprung mass m_c and four unsprung masses (two front wheels, each of mass m_{r1}, and two rear wheels, each of mass m_{r2}). In addition to the heave motion, the pitch motion of the body, and the vertical displacements of the wheel centers, the roll motion of the body is also considered. To this end, two rotating frames attached to the vehicle are defined with respect to the road-fixed frame $\mathcal{R}_0(O, \overrightarrow{x_0}, \overrightarrow{y_0}, \overrightarrow{z_0})$: the body–pitch frame $\mathcal{R}_1(G_c, \overrightarrow{x_1}, \overrightarrow{y_1}, \overrightarrow{z_1})$ and the body–roll frame $\mathcal{R}_2(G_c, \overrightarrow{x_2}, \overrightarrow{y_2}, \overrightarrow{z_2})$. The vehicle body, of mass m_c, is located by its center of gravity G. Its motion relative to the road is characterized by three translational motions: a translation along the x axis corresponding to the forward motion, a translation along the y axis corresponding to sideslip or drift, and a translation along the z axis corresponding to heave. These three translational motions are supplemented by two rotational motions: pitch, denoted θ; and roll, denoted φ. The longitudinal speed of the vehicle v is assumed to be constant throughout the motion, and the drift motion is neglected.

***Body–pitch frame*:** The body–pitch frame $\mathcal{R}_1(G_c, \overrightarrow{x_1}, \overrightarrow{y_1}, \overrightarrow{z_1})$ is obtained by a rotation through an angle θ about $\overrightarrow{y_1} = \overrightarrow{y_0}$, corresponding to the pitch motion. This motion is illustrated in Figure 1, where the plane rotation used for the projections is also defined.

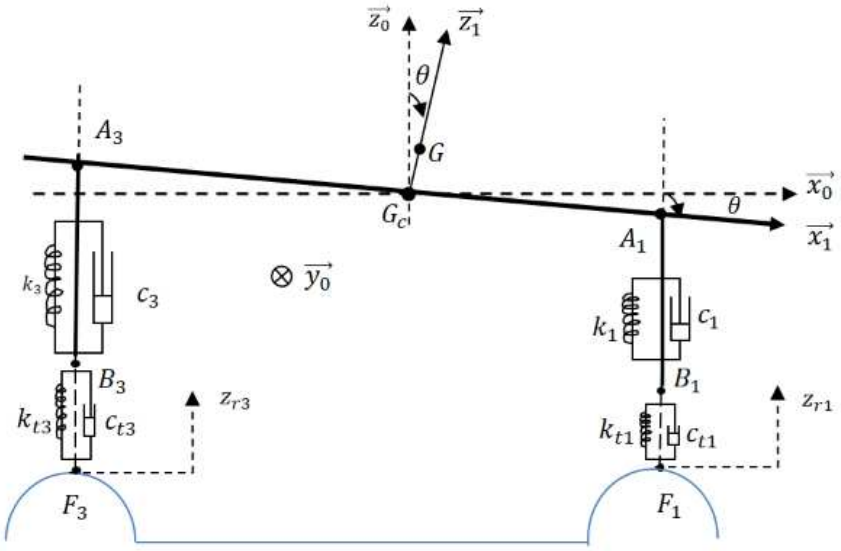


Figure 1 Pitch motion of the vehicle body (side view)

The distances $\|\overrightarrow{A_3G_c}\| = L_2$ and $\|\overrightarrow{A_1G_c}\| = L_1$ correspond to the half-wheelbases of the vehicle. We also define $\|\overrightarrow{GG_c}\| = h_G$ (the distance separating G, the centre of gravity of the body, from its orthogonal projection G_c onto the bottom of the body). The quantities $z_{r3}(t)$ and $z_{r1}(t)$ denote respectively the heights of the contact points of wheels 3 and 1 with the road surface.

Body–roll frame: This frame is denoted $\mathcal{R}_2(G_c, \overrightarrow{x_2}, \overrightarrow{y_2}, \overrightarrow{z_2})$. It is obtained by a rotation through an angle φ about $\overrightarrow{x_2} = \overrightarrow{x_1}$, corresponding to the roll motion. This motion is illustrated in Figure 2, where the plane rotation used for the projections is shown. The quantities $z_{r3}(t)$ and $z_{r4}(t)$ denote respectively the heights of the contact points of wheels 3 and 4 with the road surface.

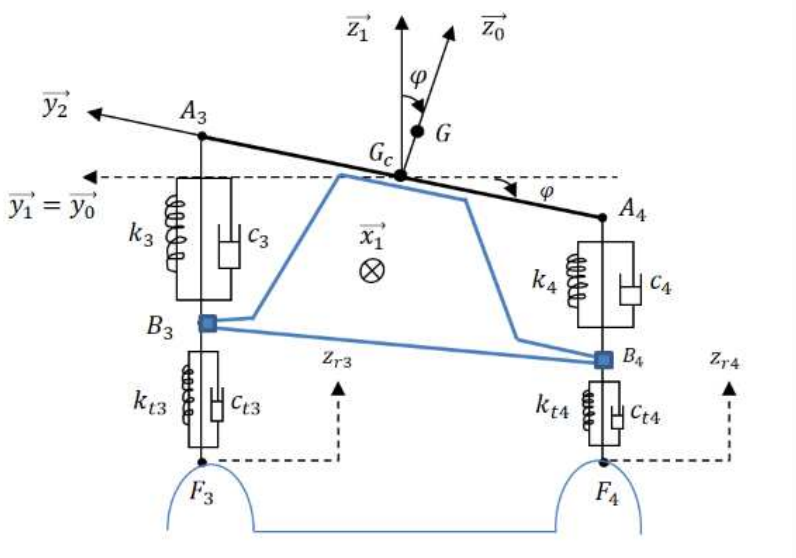


Figure 2 Roll motion of the vehicle body (rear view)

Angular velocity vector: The angular velocity of the vehicle body is defined by the composition of its rotational motions (pitch and roll) (see Figures 1 and 2). The vehicle body is located in $\mathcal{R}_0$ by the coordinates of the center of gravity G. The distance between G, the center of gravity of the vehicle body, and its orthogonal projection G_c onto the lower part of the body is denoted h_G. All the rotation axes are assumed to pass through the point G_c. Thus, the angular velocity vector $\vec{\Omega}(\Sigma_s/\mathcal{R}_0)$ of the body is given by:

$$\vec{\Omega}(\Sigma_s/\mathcal{R}_0)\big|_{\mathcal{R}_3} = \dot{\varphi}\overrightarrow{x_1} + (\dot{\theta}\, cos\, \varphi)\overrightarrow{y_2} - (\dot{\theta}\, sin\, \varphi)\overrightarrow{z_2} \quad (1)\ ,$$

where Σ_s denotes the full vehicle.

The expression of $\vec{\Omega}(\Sigma_s/\mathcal{R}_0)$ in the frame $\mathcal{R}_2$ makes it possible to compute the rotational kinetic energy of the rigid body about its center of gravity G, since the inertia matrix at G is expressed in this frame. Moreover, this angular velocity vector also allows the velocity of any point of the rigid body to be expressed, once the velocity of one point of the body is known. In that case, it is expressed in one of the appropriate bases.

Position vector: From the definition of the various translational motions of the vehicle body, the position of G in $\mathcal{R}_0$ is given by:

$$\overrightarrow{OG} = \overrightarrow{OG_c} + \overrightarrow{G_cG} \quad (2)\ ,$$

with

$$\overrightarrow{OG_c} = x\overrightarrow{x_0} + z\overrightarrow{z_0} \text{ and } \overrightarrow{\mathrm{G_cG}} = h_G\overrightarrow{z_2}$$

where x is the advance and z is the heave of the vehicle model.

Taking this expression into account, relation (2) giving the position of the centre of gravity of the vehicle in the absolute frame $\mathcal{R}_0$ is finally obtained as

$$\overrightarrow{OG} = (x + h_G \cos\varphi \sin\theta)\overrightarrow{x_0} - h_G \sin\varphi \overrightarrow{y_0} + (z + h_G \cos\varphi \cos\theta)\overrightarrow{z_0} \quad (3)\ ,$$

Instantaneous velocity vector: The instantaneous velocity vector of the vehicle body defined in this section is the derivative of the position vector $\overrightarrow{OG}$ with respect to time t in the frame $\mathcal{R}_0$. After computation, its expression is given by:

$$\vec{V}(\mathrm{G} \in \mathcal{R}_2)\big|_{\mathcal{R}_0} = \begin{Bmatrix} \dot{x} - h_G(\dot{\varphi}\sin\varphi\sin\theta - \dot{\theta}\cos\varphi\cos\theta) \\ -h_G\dot{\varphi}\cos\varphi \\ \dot{z} - h_G(\dot{\varphi}\sin\varphi\cos\theta + \dot{\theta}\sin\theta\cos\varphi) \end{Bmatrix}_{\mathcal{R}_0} \quad (4)\ ,$$

Equations of motion: The vehicle considered is a full model, allowing analysis of the body's pitch, heave, and roll motions, as well as the vertical displacements of the wheels.

The inertia matrix of the system (Σ_s), expressed in the vehicle-fixed frame $\mathcal{R}_2$ at its centre of gravity G, is given by:

$$J_s(G, m_c) = \begin{pmatrix} J_{xx} & 0 & -J_{xz} \\ 0 & J_{yy} & 0 \\ -J_{zx} & 0 & J_{zz} \end{pmatrix}_{\mathcal{R}_2} \quad (5)\ ,$$

where J_{xx}, J_{yy}, J_{zz} and J_{zx} denote respectively the moment of inertia about the x, y and z axes and the product of inertia associated with the roll-yaw coupling, all expressed in kg·m².

The products of inertia $J_{xy} = J_{yx}$ and $J_{yz} = J_{zy}$ vanish owing to material symmetry [14]. Indeed, the vertical plane $(\mathrm{x_1Gz_2})$ is a plane of symmetry of the body. This left–right symmetry is common to both vehicles (symmetric and asymmetric) studied in Section 5. In this study, the distinction between the symmetric and asymmetric vehicles concerns the front–rear symmetry: the symmetric vehicle is front–rear symmetric, whereas the so-called asymmetric vehicle is not. It is further assumed that this front–rear symmetry or asymmetry affects only the equality (or not) of the half-wheelbases and the characteristics of the front and rear suspensions. Moreover, the product of inertia J_{xz}, which might remain nonzero for the asymmetric vehicle, is also neglected in what follows.
Finally, the kinetic energy of the vehicle system can be written as:

$$\begin{aligned} T(\Sigma_s/\mathcal{R}_0) = {} & \frac{1}{2}m_c(\dot{x}^2 + \dot{z}^2) + \frac{1}{2}\left[\left(m_c h_G^2 + J_{yy}\right)\cos^2\varphi + J_{zz}\sin^2\varphi\right]\dot{\theta}^2 \\ & - m_c h_G\left[(\dot{x}\sin\theta + \dot{z}\cos\theta)\dot{\varphi}\sin\varphi + (\dot{x}\cos\theta - \dot{z}\sin\theta)\dot{\theta}\cos\varphi\right] \\ & + \frac{1}{2}(m_c h_G^2 + J_{xx})\dot{\varphi}^2 + (m_{r1} + m_{r2})\dot{x}^2 + \frac{1}{2}m_{r1}(\dot{z}_1^2 + \dot{z}_2^2) \\ & + \frac{1}{2}m_{r2}(\dot{z}_3^2 + \dot{z}_4^2) \end{aligned} \quad (6)\ ,$$

Where m_c represents the sprung mass, and m_{r1} and m_{r2} the unsprung masses of the front and rear wheels, respectively.

Crossing a speed bump by a wheel: The suspension spring transmits no horizontal component to the vehicle body, since its connection point to the chassis is generally a joint. The transmitted force acts only in the vertical direction, at the articulation point of wheel B_i. The suspensions are modeled by passive

springs and dampers. For each suspension i of axle j, the elastic force of the spring $F_{k_j}^i$ and the damping force $F_{c_j}^i$ in the suspension-fixed frame are given by:

$$\begin{cases} F_{k_j}^i = k_j d_i \\ F_{c_j}^i = c_j \dot{d}_i \end{cases}, \qquad i = \overline{1,4} \; and \; j = 1,2 \tag{7}$$

with

$$\begin{cases} d_i = z - z_i + (-1)^j L_j \cos\varphi \sin\theta - (-1)^i E^* \sin\varphi \\ \dot{d}_i = \dot{z} - \dot{z}_i + (-1)^j L_j \left(-\dot{\varphi} \sin\varphi \sin\theta + \dot{\theta} \cos\varphi \cos\theta\right) - (-1)^i E^* \dot{\varphi} \cos\varphi \end{cases} \tag{8}$$

where

- k_j is the spring stiffness of axle *j*;
- c_j is the damping coefficient of axle *j*;
- z is the vertical displacement of the body;
- z_i is the vertical displacement of the center of wheel *i*;
- θ is the pitch angle of the body;
- φ is the roll angle of the body;
- L_j is the half-wheelbase (front or rear);
- E is the track (front or rear) and E^* the half- track;
- *i* is the index of the four wheels of the full vehicle;
- *j* is the index of the two axles of the full vehicle.

The dynamic equations of the full vehicle model are given by:

$$\begin{aligned} & m_c \ddot{z} - m_c h_G \left(\ddot{\varphi} \cos\theta \sin\varphi + \dot{\varphi}^2 \cos\theta \cos\varphi - \ddot{\theta} \sin\theta \cos\varphi - \dot{\theta}^2 \cos\theta \cos\varphi\right) \\ & \qquad + k_1(d_1 + d_2) + k_2(d_3 + d_4) + c_1\left(\dot{d}_1 + \dot{d}_2\right) + c_2\left(\dot{d}_3 + \dot{d}_4\right) = 0 \end{aligned} \tag{9}$$

$$\begin{aligned} & \left[\left(J_{yy} + m_c h_G^2\right)\cos^2\varphi + J_{zz}\sin^2\varphi\right]\ddot{\theta} - \left(m_c h_G^2 + J_{yy} - J_{zz}\right)\dot{\theta}\sin 2\varphi \\ & \qquad - m_c h_G\left(-\dot{x}\dot{\theta}\sin\theta - \ddot{z}\sin\theta - \dot{z}\dot{\theta}\cos\theta\right)\cos\varphi \\ & \qquad + m_c h_G \dot{\varphi}(\dot{x}\cos\theta - \dot{z}\sin\theta)\sin\varphi \\ & \qquad + m_c h_G\left[(\dot{x}\cos\theta - \dot{z}\sin\theta)\dot{\varphi}\sin\varphi - (\dot{x}\sin\theta + \dot{z}\cos\theta)\dot{\theta}\cos\varphi\right] \\ & \qquad - k_1 L_1(d_1 + d_2)\cos\varphi\cos\theta + k_2 L_2(d_3 + d_4)\cos\varphi\cos\theta \\ & \qquad - c_1 L_1\left(\dot{d}_1 + \dot{d}_2\right)\cos\varphi\cos\theta + c_2 L_2\left(\dot{d}_3 + \dot{d}_4\right)\cos\varphi\cos\theta = 0 \end{aligned} \tag{10}$$

$$\begin{aligned} & \left(J_{xx} + m_c h_G^2\right)\ddot{\varphi} - m_c h_G(\dot{x}\sin\theta + \dot{z}\cos\theta)\dot{\varphi}\cos\varphi \\ & \qquad - m_c h_G\left(\dot{x}\dot{\theta}\cos\theta + \ddot{z}\cos\theta - \dot{z}\dot{\theta}\sin\theta\right)\sin\varphi \\ & \qquad + \frac{1}{2}\left(m_c h_G^2 + J_{yy} - J_{zz}\right)\dot{\theta}^2\sin 2\varphi + c_{\varphi_r}\dot{\varphi}^r + k_{\varphi_f}\varphi^f + k_{\varphi_r}\varphi^r \\ & \qquad + m_c h_G\left[(\dot{x}\sin\theta + \dot{z}\cos\theta)\dot{\varphi}\cos\varphi - (\dot{x}\cos\theta - \dot{z}\sin\theta)\dot{\theta}\sin\varphi\right] \\ & \qquad + k_1[(L_1\sin\varphi\sin\theta + E^*\cos\varphi)d_1 + (L_1\sin\varphi\sin\theta - E^*\cos\varphi)d_2] \\ & \qquad + k_2[(-L_2\sin\varphi\sin\theta + E^*\cos\varphi)d_3 + (-L_2\sin\varphi\sin\theta - E^*\cos\varphi)d_4] \\ & \qquad + c_1 L_1\left[(L_1\sin\varphi\sin\theta + E^*\cos\varphi)\dot{d}_1 + (L_1\sin\varphi\sin\theta - E^*\cos\varphi)\dot{d}_2\right] \\ & \qquad + c_2 L_2\left[(-L_2\sin\varphi\sin\theta - E^*\cos\varphi)\dot{d}_3 + (L_1\sin\varphi\sin\theta + E^*\cos\varphi)\dot{d}_4\right] \\ & \qquad + c_{\varphi_f}\dot{\varphi}^f = 0 \end{aligned} \tag{11}$$

$$m_{r1}\ddot{z}_1 - \left(k_1 d_1 + c_1 \dot{d}_1\right) + \left[k_{t1}(z_1 - z_{r1}) + c_{t1}(\dot{z}_1 - \dot{z}_{r1})\right] + c_{\varphi_r}\frac{\partial \dot{\varphi}^r}{\partial \dot{z}_1} + k_{\varphi_r}\frac{\partial \varphi^r}{\partial z_1} = 0 \tag{12}$$

$$m_{r1}\ddot{z}_2 - \left(k_1 d_2 + c_1 \dot{d}_2\right) + \left[k_{t1}(z_2 - z_{r2}) + c_{t1}(\dot{z}_2 - \dot{z}_{r2})\right] + c_{\varphi_r}\frac{\partial \dot{\varphi}^r}{\partial \dot{z}_2} + k_{\varphi_r}\frac{\partial \varphi^r}{\partial z_2} = 0 \tag{13}$$

$$m_{r2}\ddot{z}_3 - \left(k_2 d_3 + c_2 \dot{d}_3\right) + \left[k_{t2}(z_3 - z_{r3}) + c_{t2}(\dot{z}_3 - \dot{z}_{r3})\right] + c_{\varphi_f}\frac{\partial \dot{\varphi}^f}{\partial \dot{z}_3} + k_{\varphi_f}\frac{\partial \varphi^f}{\partial z_3} = 0 \tag{14}$$

and,

$$m_{r2}\ddot{z}_4 - \left(k_2 d_4 + c_2 \dot{d}_4\right) + \left[k_{t2}(z_4 - z_{r4}) + c_{t2}(\dot{z}_4 - \dot{z}_{r4})\right] + c_{\varphi_f}\frac{\partial \dot{\varphi}^f}{\partial \dot{z}_4} + k_{\varphi_f}\frac{\partial \varphi^f}{\partial z_4} = 0 \tag{15}$$

where k_{t1} and k_{t2} are the vertical stiffness of one front and rear tyre, c_{t1} and c_{t2} are the damping coefficient of one front and rear tyre , k_{φ_f} and k_{φ_r} are the torsional stiffness coefficient of the front and rear anti-roll bars, and c_{φ_f} and c_{φ_r} are the torsional damping coefficient of the front and rear anti-roll bars.

The anti-roll angles for the front and rear wheels, respectively, are given by [15]:

$$\begin{cases} \varphi^f = tan^{-1}\left(\dfrac{z_1 - z_2}{E}\right) - \varphi \\ \varphi^r = tan^{-1}\left(\dfrac{z_3 - z_4}{E}\right) - \varphi \end{cases} \tag{16}$$

These angles represent the relative rotational motion between the vehicle body and the axles.

3. Modeling of the speed bump

Finding a highly realistic mathematical model to describe road surface profiles is complex, if possible at all, as pointed out by Ata et al. [16]. Consequently, the literature offers several approaches for the mathematical modelling of the road surface: [1,11,12,16–24]. For instance, in works by Ata et al. [16] and Mohammadzadeh et al. [25], the road surface is modeled using a trigonometric function to represent a speed bump. In other works, such as Davis et al. [17], ISO 8608 [18], Bouazara [19], Robson [12], Dodds et al. [11], and Kropáč et al. [20], the road surface is described by means of a power spectral density (PSD). Lombaert et al. [23] propose a piecewise-defined function, whereas Danho et al. [26] use a function defined by the characteristic equation of an ellipse. Other models are also mentioned: a discrete function in Garcia-Pozuelo et al. [24], a circular function in Danho et al. [1], and a pothole-modeling example in Pesterev et al. [27].

Road modeling: The vertical height of wheel 1 (front left wheel) when crossing a hump-type speed bump is given by:

$$z_{r1}(t) = \begin{cases} \dfrac{h_0}{2}\left[1 - \cos\left(\dfrac{2\pi v(t - t_1)}{l_b}\right)\right] & if \quad t_1 \le t \le t_2 \\ 0 & otherwise \end{cases} \tag{17}$$

where

$$t_1 = \frac{L_e}{v}, \quad t_2 = t_1 + \frac{l_b}{v} \; and \; t_\delta = \frac{L_1 + L_2}{v}$$

with

- h_0 : height of the speed bump;
- t_1 : starting time of the speed bump
- t_2 : ending time of the speed bump
- t_δ : time delay due to the total wheelbase of the vehicle
- t_{ec} : time delay of the front right wheel with respect to the front left wheel when reaching the oblique speed bump
- L_e : Distance between the origin and the approach point of the first speed bump.
- l_b : width of the speed bump
- l_{ec} : longitudinal offset between the point at which the left wheel meets the obstacle and the point at which the right wheel of the same axle meets it (Figure 3.b).
- v : magnitude of the longitudinal speed of the vehicle.

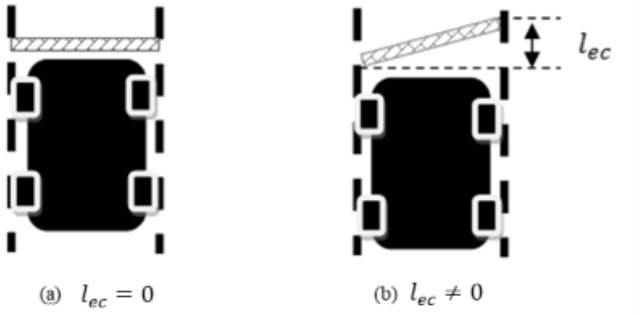


Figure 3 Speed bump with an orthogonal axis (a) and with an oblique axis (b) with respect to the longitudinal axis of the vehicle [28].

Thus, according to relation (17), the excitations of the various wheels of the vehicle (Figure 3), taking its geometry into account, are:

- wheel 1 : $z_{r1}(t)$
- wheel 2 : $z_{r2}(t) = z_{r1}(t - t_{ec})$
- wheel 3 : $z_{r3}(t) = z_{r1}(t - t_\delta)$
- wheel 4 : $z_{r4}(t) = z_{r1}(t - t_{ec} - t_\delta)$

It is assumed in this study that $l_{ec} < L_1 + L_2$, that is, no two wheels of the vehicle reach the speed bump at the same instant.

4. Linearized dynamic equations

The dynamic equations obtained are strongly nonlinear. The roll and pitch angles are assumed to remain small, which makes it possible to "linearize" the trigonometric functions and to retain only the terms of order less than or equal to 3 which, once differentiated, yield terms of order at most equal to 2. Thus, taking this assumption into account, we define the linearized equations of the dynamic system.

$$\begin{aligned} m_c\ddot{z} + 2(c_1 + c_2)\dot{z} + 2(c_2L_2 - c_1L_1)\dot{\theta} - c_1\dot{z}_1 - c_1\dot{z}_2 - c_2\dot{z}_3 - c_2\dot{z}_4 + 2(k_1 + k_2)z \\ + 2(k_2L_2 - k_1L_1)\theta - k_1z_1 - k_1z_2 - k_2z_3 - k_2z_4 = 0 \end{aligned} \tag{18}$$

$$\begin{aligned}\left(J_{yy}+m_c h_G^2\right)\ddot{\theta}\ &+2(c_2L_2-c_1L_1)\dot{z}+2(c_2L_2^2+c_1L_1^2)\dot{\theta}+c_1L_1\dot{z}_1+c_1L_1\dot{z}_2-c_2L_2\dot{z}_3\\&-c_2L_2\dot{z}_4+2(k_2L_2-k_1L_1)z+2(k_2L_2^2+k_1L_1^2)\theta+k_1L_1z_1+k_1L_1z_2\\&-k_2L_2z_3-k_2L_2z_4=0\end{aligned}\tag{19}$$

$$\begin{aligned}(J_{xx}+m_c h_G^2)\ddot{\varphi}\ &+\left[c_{\varphi_f}+c_{\varphi_r}+2(c_1+c_2)E^{*2}\right]\dot{\varphi}-\left(c_1E^*+\frac{c_{\varphi_f}}{E}\right)\dot{z}_1+\left(c_1E^*+\frac{c_{\varphi_f}}{E}\right)\dot{z}_2\\&-\left(c_2E^*+\frac{c_{\varphi_r}}{E}\right)\dot{z}_3+\left(c_2E^*+\frac{c_{\varphi_r}}{E}\right)\dot{z}_4+\left[k_{\varphi_f}+k_{\varphi_r}+2(k_1+k_2)E^{*2}\right]\varphi\\&-\left(k_1E^*+\frac{k_{\varphi_f}}{E}\right)z_1+\left(k_1E^*+\frac{k_{\varphi_f}}{E}\right)z_2-\left(k_2E^*+\frac{k_{\varphi_r}}{E}\right)z_3\\&+\left(k_2E^*+\frac{k_{\varphi_r}}{E}\right)z_4=0\end{aligned}\tag{20}$$

$$\begin{aligned}m_{r1}\ddot{z}_1-c_1\dot{z}+c_1L_1\dot{\theta}-\left(c_1E^*+\frac{c_{\varphi_f}}{E}\right)\dot{\varphi}+\left(c_1+c_{t1}+\frac{c_{\varphi_f}}{E^2}\right)\dot{z}_1-\frac{c_{\varphi_f}}{E^2}\dot{z}_2-k_1z+k_1L_1\theta\\-\left(k_1E^*+\frac{k_{\varphi_f}}{E}\right)\varphi+\left(k_1+\frac{k_{\varphi_f}}{E^2}+k_{t1}\right)z_1-\frac{k_{\varphi_f}}{E^2}z_2=c_{t1}\dot{z}_{r1}+k_{t1}z_{r1}\end{aligned}\tag{21}$$

$$\begin{aligned}m_{r1}\ddot{z}_2-c_1\dot{z}+c_1L_1\dot{\theta}+\left(c_1E^*+\frac{c_{\varphi_f}}{E}\right)\dot{\varphi}-\frac{c_{\varphi_f}}{E^2}\dot{z}_1+\left(c_1+c_{t1}+\frac{c_{\varphi_f}}{E^2}\right)\dot{z}_2-k_1z+k_1L_1\theta\\+\left(k_1E^*+\frac{k_{\varphi_f}}{E}\right)\varphi-\frac{k_{\varphi_f}}{E^2}z_1+\left(k_1+k_{t1}+\frac{k_{\varphi_f}}{E^2}\right)z_2=c_{t1}\dot{z}_{r2}+k_{t1}z_{r2}\end{aligned}\tag{22}$$

$$\begin{aligned}m_{r2}\ddot{z}_3-c_2\dot{z}-c_2L_2\dot{\theta}-\left(c_2E^*+\frac{c_{\varphi_r}}{E}\right)\dot{\varphi}+\left(c_2+c_{t2}+\frac{c_{\varphi_r}}{E^2}\right)\dot{z}_3-\frac{c_{\varphi_r}}{E^2}\dot{z}_4-k_2z-k_2L_2\theta\\-\left(k_2E^*+\frac{k_{\varphi_r}}{E}\right)\varphi+\left(k_2+k_{t2}+\frac{k_{\varphi_r}}{E^2}\right)z_3-\frac{k_{\varphi_r}}{E^2}z_4=c_{t2}\dot{z}_{r3}+k_{t2}z_{r3}\end{aligned}\tag{23}$$

$$\begin{aligned}m_{r2}\ddot{z}_4-c_2\dot{z}-c_2L_2\dot{\theta}+\left(c_2E^*+\frac{c_{\varphi_r}}{E}\right)\dot{\varphi}-\frac{c_{\varphi_r}}{E^2}\dot{z}_3+\left(c_2+c_{t2}+\frac{c_{\varphi_r}}{E^2}\right)\dot{z}_4-k_2z-k_2L_2\theta\\+\left(k_2E^*+\frac{k_{\varphi_r}}{E}\right)\varphi-\frac{k_{\varphi_r}}{E^2}z_3+\left(k_2+k_{t2}+\frac{k_{\varphi_r}}{E^2}\right)z_4=c_{t2}\dot{z}_{r4}+k_{t2}z_{r4}\end{aligned}\tag{24}$$

and one obtains, like in [7,29,30]:

$$\boldsymbol{M\ddot{q}+C\dot{q}+Kq=K_tX+C_t\dot{X}}\tag{25}$$

where $\boldsymbol{M}$, $\boldsymbol{C}$, $\boldsymbol{C_t}$, $\boldsymbol{K}$, $\boldsymbol{K_t}$ are respectively the mass matrix of the vehicle system, the damping matrix of the vehicle system, the tyre damping matrix, the stiffness matrix of the vehicle system and the tyre stiffness matrix; $\boldsymbol{q}$, $\boldsymbol{X}$ and $\boldsymbol{F}$ are respectively the generalized displacement, the excitation and the generalized force vectors; $\dot{\boldsymbol{q}}$ is a generalized velocity vector and $\ddot{\boldsymbol{q}}$ is a generalized acceleration vector,
with

$$\boldsymbol{q}^T=[z\quad\theta\quad\varphi\quad z_1\quad z_2\quad z_3\quad z_4],\qquad \boldsymbol{X^T}=[z_{r1}\quad z_{r2}\quad z_{r3}\quad z_{r4}]$$

$$\boldsymbol{M} = \begin{bmatrix} m_c & 0 & 0 & 0 & 0 & 0 & 0 \\ 0 & (J_{yy} + m_c h_G^2) & 0 & 0 & 0 & 0 & 0 \\ 0 & 0 & (J_{xx} + m_c h_G^2) & 0 & 0 & 0 & 0 \\ 0 & 0 & 0 & m_{r1} & 0 & 0 & 0 \\ 0 & 0 & 0 & 0 & m_{r1} & 0 & 0 \\ 0 & 0 & 0 & 0 & 0 & m_{r2} & 0 \\ 0 & 0 & 0 & 0 & 0 & 0 & m_{r2} \end{bmatrix},$$

$$\boldsymbol{K_t} = \begin{bmatrix} 0 & 0 & 0 & 0 \\ 0 & 0 & 0 & 0 \\ 0 & 0 & 0 & 0 \\ k_{t1} & 0 & 0 & 0 \\ 0 & k_{t1} & 0 & 0 \\ 0 & 0 & k_{t2} & 0 \\ 0 & 0 & 0 & k_{t2} \end{bmatrix}, \quad \boldsymbol{C_t} = \begin{bmatrix} 0 & 0 & 0 & 0 \\ 0 & 0 & 0 & 0 \\ 0 & 0 & 0 & 0 \\ c_{t1} & 0 & 0 & 0 \\ 0 & c_{t1} & 0 & 0 \\ 0 & 0 & c_{t2} & 0 \\ 0 & 0 & 0 & c_{t2} \end{bmatrix}$$

$$\boldsymbol{K} = \begin{bmatrix} 2(k_1+k_2) & 2(k_2L_2-k_1L_1) & 0 & -k_1 & -k_1 & -k_2 & -k_2 \\ 2(k_2L_2-k_1L_1) & 2(k_2L_2^2+k_1L_1^2) & 0 & k_1L_1 & k_1L_1 & -k_2L_2 & -k_2L_2 \\ 0 & 0 & K_{33} & -\left(k_1E^*+\frac{k_{\varphi_f}}{E}\right) & \left(k_1E^*+\frac{k_{\varphi_f}}{E}\right) & -\left(k_2E^*+\frac{k_{\varphi_r}}{E}\right) & \left(k_2E^*+\frac{k_{\varphi_r}}{E}\right) \\ -k_1 & k_1L_1 & -\left(k_1E^*+\frac{k_{\varphi_f}}{E}\right) & K_{44} & -\frac{k_{\varphi_f}}{E^2} & 0 & 0 \\ -k_1 & k_1L_1 & \left(k_1E^*+\frac{k_{\varphi_f}}{E}\right) & -\frac{k_{\varphi_f}}{E^2} & K_{55} & 0 & 0 \\ -k_2 & -k_2L_2 & -\left(k_2E^*+\frac{k_{\varphi_r}}{E}\right) & 0 & 0 & K_{66} & -\frac{k_{\varphi_r}}{E^2} \\ -k_2 & -k_2L_2 & \left(k_2E^*+\frac{k_{\varphi_r}}{E}\right) & 0 & 0 & -\frac{k_{\varphi_r}}{E^2} & K_{77} \end{bmatrix}$$

$$\boldsymbol{C} = \begin{bmatrix} 2(c_1+c_2) & 2(c_2L_2-c_1L_1) & 0 & -c_1 & -c_1 & -c_2 & -c_2 \\ 2(c_2L_2-c_1L_1) & 2(c_2L_2^2+c_1L_1^2) & 0 & c_1L_1 & c_1L_1 & -c_2L_2 & -c_2L_2 \\ 0 & 0 & C_{33} & -\left(c_1E^*+\frac{c_{\varphi_f}}{E}\right) & \left(c_1E^*+\frac{c_{\varphi_f}}{E}\right) & -\left(c_2E^*+\frac{c_{\varphi_r}}{E}\right) & \left(c_2E^*+\frac{c_{\varphi_r}}{E}\right) \\ -c_1 & c_1L_1 & -\left(c_1E^*+\frac{c_{\varphi_f}}{E}\right) & C_{44} & -\frac{c_{\varphi_f}}{E^2} & 0 & 0 \\ -c_1 & c_1L_1 & \left(c_1E^*+\frac{c_{\varphi_f}}{E}\right) & -\frac{c_{\varphi_f}}{E^2} & C_{55} & 0 & 0 \\ -c_2 & -c_2L_2 & -\left(c_2E^*+\frac{c_{\varphi_r}}{E}\right) & 0 & 0 & C_{66} & -\frac{c_{\varphi_r}}{E^2} \\ -c_2 & -c_2L_2 & \left(c_2E^*+\frac{c_{\varphi_r}}{E}\right) & 0 & 0 & -\frac{c_{\varphi_r}}{E^2} & C_{77} \end{bmatrix}$$

with

$$K_{33} = k_{\varphi_f} + k_{\varphi_r} + 2(k_1+k_2)E^{*2}\,;\; K_{44} = K_{55} = \left(k_1 + k_{t1} + \frac{k_{\varphi_f}}{E^2}\right);\; K_{66} = K_{77} = \left(k_2 + k_{t2} + \frac{k_{\varphi_r}}{E^2}\right)$$

$$C_{33} = c_{\varphi_f} + c_{\varphi_r} + 2(c_1+c_2)E^{*2}\,;\; C_{44} = C_{55} = \left(c_1 + c_{t1} + \frac{c_{\varphi_f}}{E^2}\right);\; C_{66} = C_{77} = \left(c_2 + c_{t2} + \frac{c_{\varphi_r}}{E^2}\right)$$

5. Mode shapes and natural frequencies

In the dynamic analysis of mechanical systems, particularly in linear vehicle dynamics, determining the natural frequencies is a fundamental step in characterizing the vibration modes associated with the various degrees of freedom. These frequencies, obtained from the eigenvalue problem associated with the system, represent the natural responses of the structure in the absence of external excitation. However, beyond their mere identification, particular attention must be paid to possible frequency coincidences [7].

In complex mechanical systems such as road vehicles, such coincidences may lead to significant interactions between apparently independent motions (for example, heave, roll, and pitch), resulting in amplified vibrations or counterintuitive dynamic responses in the random vibration setting. Thus, an excitation near a common frequency may activate several modes simultaneously, increasing the risk of resonance and degrading performance in terms of stability, comfort, and road-holding. The eigenvalue problem governing these natural frequencies is given by:

$$det\ (\boldsymbol{K} - \lambda \boldsymbol{M}) = \boldsymbol{0}, \qquad \lambda = \omega_n^2 \tag{26}$$

Equation (26) is solved for two configurations of the model: the symmetric model and the asymmetric model. In all that follows, the crossing is oblique (Figure 3.b): the front right wheel reaches the speed bump with a spatial offset l_{ec} (taken equal to 0.6 m in this study) with respect to the front left wheel.

5.1 Asymmetric vehicle model

In the table below, we present the realistic asymmetric vehicle model and corresponding parameters.

Description	Symbol	Value
Unsprung mass (front/rear)	m_{r1} and m_{r2}	40/40 kg
Sprung mass	m_c	1,375.9 kg
Sprung moment of inertia about the x/y axes	J_{xx} and J_{yy}	484.4/2,344.4 kgm^2
Vertical stiffness of one tyre (front/rear)	k_{t1} and k_{t2}	182,087/182,087 N/m
Suspension stiffness per wheel (front/rear)	k_1 and k_2	20,984.8/19,121.7 N/m
Damping coefficient of one tyre (front/rear)	c_{t1} and c_{t2}	1,820.9/1,820.9 Ns/m
Suspension damping per wheel (front/rear)	c_1 and c_2	209.8/191.2 Ns/m
Distance between the x axis and the front/rear tyres	L_1 and L_2	1.125/1.511 m
Distance between the left and right tyres	E	1.44 m
Torsional stiffness coefficient of the front and rear anti-roll bars	k_{φ_f} and k_{φ_r}	62,085/58,098 N.m/rad
Torsional damping coefficient of the front and rear anti-roll bars	c_{φ_f} and c_{φ_r}	620.85/580.98N.m.s/rad

Table 1: Realistic asymmetric vehicle model and corresponding parameters [7].

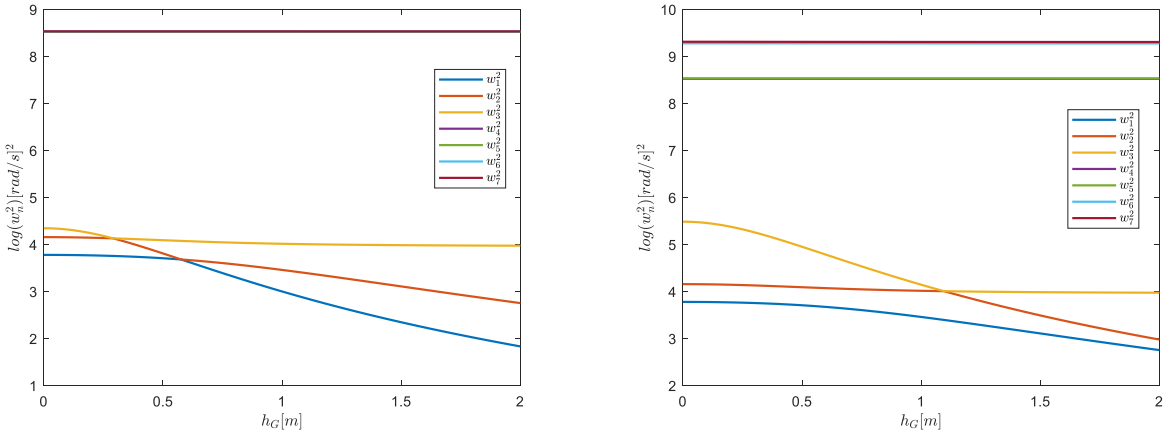


Figure 4: Squared natural frequencies of the realistic asymmetric vehicle model k_φ = 0 N m/rad (a) and $k_\varphi \neq 0$ N m/rad (b)

Figure 4 highlights the natural-frequency coincidences of the asymmetric model, and the corresponding critical values of the center-of-gravity height h_G are summarized in Table 2. The natural frequencies associated with the four wheels split into two pairs of close frequencies. In addition, changing the height of the center of gravity leads to further coincidences between the natural frequencies associated with the

body modes. More precisely, the heave and roll modes have identical frequencies whether the anti-roll stiffness is zero $(k_\varphi = 0)$ or not ($k_\varphi \neq 0$). By contrast, the coincidence between the pitch and roll modes is observed only in the absence of anti-roll stiffness.

Table 2: Realistic asymmetric vehicle model: squared natural frequencies ω_n^2, modal damping ratios ξ_n and maximal damping-coupling coefficient $\eta_{\alpha\beta}$ at the critical heights h_G of the center of gravity. (bold identifies coincident frequencies)

Torsional stiffness coefficient		**$k_\varphi = 0$**		**$k_\varphi \neq 0$**
h_G **(m)**		**0.3558544546**	**0.5217358001**	**1.0893504852**
ω_n^2 (rad²/s²)	1	**56.7889**	55.4165	**53.2856**
	2	45.8828	**43.5589**	30.9793
	3	**56.7889**	**43.5589**	**53.2856**
	4	5.0805×10^3	5.0820×10^3	6.5870×10^3
	5	5.0822×10^3	5.0796×10^3	5.0814×10^3
	6	5.0362×10^3	5.0360×10^3	6.4410×10^3
	7	5.0329×10^3	5.0323×10^3	5.0350×10^3
ξ_α	1	0.0377	0.0372	0.0365
	2	0.0339	0.0330	0.0278
	3	0.0377	0.0330	0.0365
	4	0.3564	0.3564	0.4058
	5	0.3564	0.3564	0.3564
	6	0.3548	0.3548	0.4013
	7	0.3547	0.3547	0.3548
$\eta_{\alpha\beta}$		7.4081×10^{-5}	7.1016×10^{-5}	6.0081×10^{-5}
coincidence of natural frequencies		Heave-roll	Pitch - roll	Heave-roll

where $\xi_\alpha = C_{mod,\alpha}/(2w_\alpha)$ and $\boldsymbol{C_{mod} = V^T CV}$ is the modal damping matrix ($\boldsymbol{V}$: mass-normalized modes).

$$\eta_{\alpha\beta} = \max \frac{|C_{\alpha\beta}|}{\sqrt{C_{\alpha\alpha} C_{\beta\beta}}}, \qquad \alpha \neq \beta$$

where w_α is the natural frequency associated with mode α, $C_{\alpha\beta}$ is the modal damping coupling between modes α and β,, and $C_{\alpha\alpha}$ and $C_{\beta\beta}$ are the generalized damping coefficients of modes α and β, respectively.

5.2 Symmetric vehicle model

The values presented in Tables 1 and 3 are taken from Long et al. [7]. To these initial parameters have been added the mechanical characteristics of the anti-roll bar, which allow the additional contributions to the stiffnesses and dampings, denoted k_{φ_r}, k_{φ_f}, c_{φ_r} and c_{φ_f}, to be included [31].

Description	**Symbol**	**Value**
Unsprung mass (front/rear)	m_{r1} and m_{r2}	40/40 kg
Sprung mass	m_c	1,375.9 kg
Sprung moment of inertia about the x/y axes	J_{xx} and J_{yy}	484.4/2,344.4 kgm²
Vertical stiffness of one tyre (front/rear)	k_{t1} and k_{t2}	18,208,700/18,208,700 N/m
Suspension stiffness per wheel (front/rear)	k_1 and k_2	20,984.8/20,984.8 N/m

Damping coefficient of one tyre (front/rear)	c_{t1} and c_{t2}	182,087/182,087 Ns/m
Suspension damping per wheel (front/rear)	c_1 and c_2	209.8/209.8Ns/m
Distance between the *x* axis and the front/rear tyres	L_1 and L_2	1.511/1.511 m
Distance between the left and right tyres	E	1.44 m
Torsional stiffness coefficient of the front and rear anti-roll bars	k_{φ_f} and k_{φ_r}	62,085/62,085N.m/rad
Torsional damping coefficient of the front and rear anti-roll bars	c_{φ_f} and c_{φ_r}	620.85/620.85 N.m.s/rad

Table 3: Ideal symmetric vehicle model and corresponding parameters. The values of c_{φ_f} and c_{φ_r}, which were not provided in the study by Yun et al. [15], were readjusted so as to satisfy the prescribed ratio $c/k = 0.01$. c and k are the damping and the stiffness coefficients, respectively.

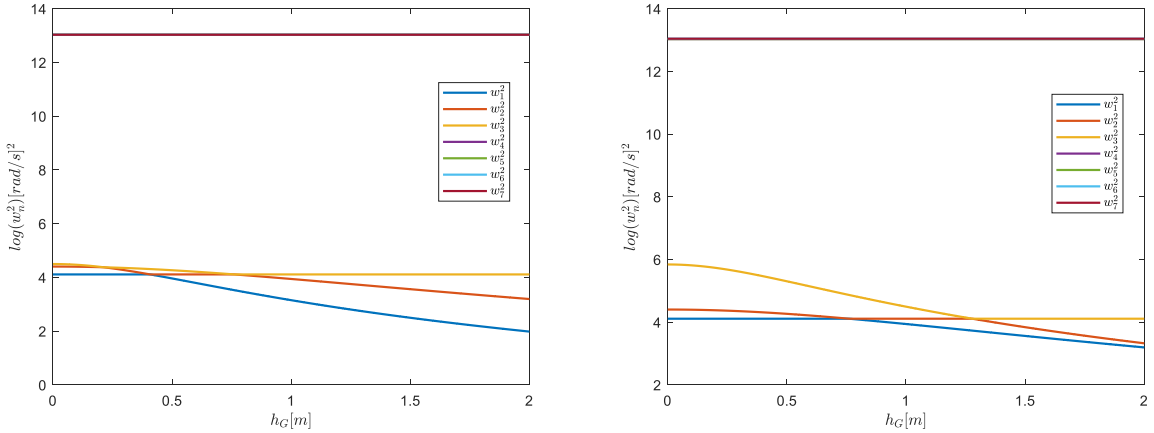


Figure 5: Squared natural frequencies of the ideal symmetric vehicle model for the following data: m_c = 1,375.9 kg, m_r = 40 kg, J_{xx} = 484.4 kg.m^2, J_{yy} = 2,344.4 kg.m^2, k = 20,984.8 N/m, k_t = 18,208,700 N/m, L = 1.511 m, E = 1.44 m, k_φ = 0 N m/rad (a) and $k_\varphi \neq 0$ N m/rad (b)

Each pair of modes has its own critical height, and h_G determines the order of the three body frequencies (Figure 5 and Table 4). As h_G increases, the pitch and roll frequencies decrease while the heave frequency remains unchanged. The four wheels have identical natural frequencies, reflecting the degeneracy of the modes associated with the unsprung masses. Three additional frequencies correspond to the global body modes: heave (bounce), pitch and roll. In this configuration, these modes remain decoupled from the wheel dynamics. When the center of gravity is offset, the modal spectrum exhibits, in addition to the wheel frequencies, two identical natural frequencies corresponding to the heave and pitch modes. IntroducingIntroducing the anti-roll bars lifts the degeneracy of the wheel modes, initially characterized by four identical natural frequencies. The pair of frequencies associated with the heave and pitch modes, however, remains unchanged, since the anti-roll stiffness (k_φ) acts exclusively on the roll dynamics.

Table 4: Ideal symmetric vehicle model: squared natural frequencies ω_n^2, modal damping ratios ξ_α and maximal damping-coupling coefficient $\eta_{\alpha\beta}$ at the critical heights h_G of the center of gravity. (bold identifies coincident frequencies)

Torsional stiffness coefficient		**$k_\varphi = 0$**			**$k_\varphi \neq 0$**	
h_G (m)		**0.2122577716**	**0.4078474349**	**0.7610637953**	**0.7610637953**	**1.280266805**
ω_n^2 (rad²/s²)	1	60.9365	**60.9365**	**60.9365**	**60.9365**	**60.9365**
	2	**79.5477**	74.3890	**60.9365**	**60.9365**	41.6171
	3	**79.5477**	**60.9365**	33.9206	130.2868	**60.9365**
	4	**4.5574×10^5**	**4.5574×10^5**	**4.5574×10^5**	4.5574×10^5	4.5574×10^5

	5	**4.5574 × 10^5**	**4.5574 × 10^5**	**4.5574 × 10^5**	4.5724 × 10^5	4.5724 × 10^5
	6	**4.5574 × 10^5**	**4.5574 × 10^5**	**4.5574 × 10^5**	4.5724 × 10^5	4.5574 × 10^5
	7	**4.5574 × 10^5**	**4.5574 × 10^5**	**4.5574 × 10^5**	4.5574 × 10^5	4.5724 × 10^5
	1	0.0390	0.0390	0.0390	0.0390	0.0390
	2	0.0446	0.0431	0.0390	0.0390	0.0322
	3	0.0446	0.0390	0.0291	0.0571	0.0390
ξ_α	4	3.3754	3.3754	3.3754	3.3754	3.3754
	5	3.3754	3.3754	3.3754	3.3810	3.3810
	6	3.3754	3.3754	3.3754	3.3810	3.3754
	7	3.3754	3.3754	3.3754	3.3754	3.3810
$\eta_{\alpha\beta}$		7.7581 × 10^{-6}	7.7584 × 10^{-6}	7.7577 × 10^{-6}	5.5441 × 10^{-6}	7.7581 × 10^{-6}
coincidence of natural frequencies		Pitch – roll	Heave – roll	Heave – pitch	Heave – pitch	Heave – roll

Tables 2 and 4 give the modal damping ratios and the maximum normalized modal coupling coefficients for the two vehicle configurations studied: the ideal symmetric model and the realistic asymmetric model. The results show that the maximum modal coupling $\eta_{\alpha\beta}$ remains very small for all the configurations considered, with values between 7.7584 × 10^{-6} and 7.4081 × 10^{-5}. For the realistic asymmetric model, the maximum coefficient reaches only 7.4081 × 10^{-5}, despite the absence of anti-roll stiffness. Introducing a longitudinal offset of the center of gravity and/or an anti-roll stiffness changes the level of modal coupling only marginally. Although some configurations show slightly higher coefficients than the other cases, these values remain very small. The modal damping matrix $\boldsymbol{V^T C V}$, where $\boldsymbol{V}$ denotes the modal matrix, can therefore be regarded as nearly diagonal. It is thus reasonable to neglect its off-diagonal terms in the modal projection, which leads to a system of approximately decoupled modal equations. This approximation is adopted in the remainder of the study.
When this approximation is not valid, a direct approach based on the state-space representation and the Lyapunov equation can be used. This method yields the covariance matrix of the response without neglecting the damping coupling terms and without modal truncation. Zhang et al. [35] also used this approach to obtain the zeroth- and second-order spectral moments.

For specific center-of-gravity heights h_G, the modal spectrum exhibits a particular configuration in which two natural frequencies of the vehicle body coincide while the four natural frequencies of the wheels coincide with one another. The seven modes of the system then split into two degenerate eigenspaces, of multiplicities 2 and 4 respectively, and one mode associated with a simple natural frequency. This configuration is the most pronounced case of modal degeneracy among those studied. We therefore seek closed-form expressions for the critical heights h_G at which these natural-frequency coincidences occur.

Thus, by solving equation (26) and taking the symmetry of the vehicle into account, with $L = L_1 = L_2$, $k = k_1 = k_2$, $k_\varphi = k_{\varphi f} = k_{\varphi r}$, $m_r = m_{r1} = m_{r2}$ and $k_t = k_{t1} = k_{t2}$, the squares of the natural frequencies are obtained as follows:

$$\omega_1^2 = \frac{4k\,m_r + (k + k_t)\,m_c - \sqrt{\Omega_1}}{2\,m_r\,m_c}$$

$$\omega_2^2 = \frac{4kL^2\,m_r + (k + k_t)\left(J_{yy} + m_c h_G^2\right) - \sqrt{\Omega_2}}{2\,m_r\left(J_{yy} + m_c h_G^2\right)}$$

$$\omega_3^2 = \frac{\left(2k_\varphi + kE^2\right)m_r + \left(k + k_t + \frac{2k_\varphi}{E^2}\right)\left(J_{xx} + m_c h_G^2\right) - \sqrt{\Omega_3}}{2\,m_r\left(J_{xx} + m_c h_G^2\right)}$$

$$\omega_4^2 = \frac{(k+k_t)\,E^2 + 2k_\varphi}{m_r\,E^2}$$

$$\omega_5^2 = \frac{4k\,m_r + (k+k_t)\,m_c + \sqrt{\Omega_1}}{2\,m_r\,m_c}$$

$$\omega_6^2 = \frac{4kL^2\,m_r + (k+k_t)\left(J_{yy} + m_c h_G^2\right) + \sqrt{\Omega_2}}{2\,m_r\left(J_{yy} + m_c h_G^2\right)}$$

$$\omega_7^2 = \frac{\left(2k_\varphi + kE^2\right)m_r + \left(k + k_t + \frac{2k_\varphi}{E^2}\right)\left(J_{xx} + m_c h_G^2\right) + \sqrt{\Omega_3}}{2\,m_r\left(J_{xx} + m_c h_G^2\right)}$$

Where

$$\Omega_1 = [(k+k_t)\,m_c - 4k\,m_r]^2 + 16k^2\,m_c\,m_r$$

$$\Omega_2 = \left[(k+k_t)\left(J_{yy} + m_c h_G^2\right) - 4kL^2\,m_r\right]^2 + 16k^2L^2\left(J_{yy} + m_c h_G^2\right)m_r$$

$$\Omega_3 = \left[\left(2k_\varphi + kE^2\right)m_r - \left(k + k_t + \frac{2k_\varphi}{E^2}\right)\left(J_{xx} + m_c h_G^2\right)\right]^2 + 4\left(kE + \frac{2k_\varphi}{E}\right)^2\left(J_{xx} + m_c h_G^2\right)m_r$$

From the analytical expressions of the natural frequencies ω_i^2 and the coincidences between them, the following closed-form expressions are obtained for the critical heights h_G for the modes of the body and of the unsprung masses (the wheels):

$$h_G = \begin{cases} \dfrac{\sqrt{m_c\left(m_c L^2 - J_{yy}\right)}}{m_c}, & \text{if } m_c L^2 > J_{yy}\,, \quad \forall k_\varphi \qquad \textbf{(heave - pitch)} \\ \sqrt{\dfrac{E^2}{4}\,\dfrac{1 + \dfrac{2k_\varphi}{kE^2}}{1 + \dfrac{2k_\varphi}{\mathrm{A}\,E^2}} - \dfrac{J_{xx}}{m_c}}, & \text{if } \dfrac{E^2}{4}\,\dfrac{1 + \dfrac{2k_\varphi}{kE^2}}{1 + \dfrac{2k_\varphi}{\mathrm{A}\,E^2}} > \dfrac{J_{xx}}{m_c}\,, \quad \forall k_\varphi \qquad \textbf{(heave - roll)} \\ \sqrt{\dfrac{E^2 J_{yy} - 4L^2 J_{xx}}{m_c(4L^2 - E^2)}}, & \text{if } 4L^2\dfrac{J_{xx}}{J_{yy}} < E^2 < 4L^2, \quad k_\varphi = 0 \qquad \textbf{(roll - pitch)} \end{cases}$$

with

$$A = \frac{(k+k_t)\,m_c - 4k\,m_r + \sqrt{\Omega_1}}{2\,m_c}$$

6. Computation of the autocorrelation matrix $\left[\boldsymbol{R}_{\dot{\boldsymbol{q}}\,\dot{\boldsymbol{q}}}\,(\mathbf{0})\right]$

Equation (25) can be rewritten in the following matrix form:

$$\boldsymbol{M}\ddot{q} + \boldsymbol{C}\dot{q} + \boldsymbol{K}q = \boldsymbol{F}\,(t) \tag{27}$$

where $\boldsymbol{F}(t)$ denotes the vector of the external forces applied to the vehicle, induced by the contact of the wheels with the speed bump.

In this section, two types of excitation are considered for the external forces $\boldsymbol{F}(t)$. The first corresponds to stationary random processes, modeled by a white noise of constant spectral intensity S_0, following the approach of Long et al. [7]. The second concerns the crossing of a speed hump whose geometric profile is described by Equation (17). The external forces associated with these two types of excitation are written as follows:

$$\boldsymbol{F}(\boldsymbol{t}) = \begin{Bmatrix} F_1(t) \\ F_2(t) \\ F_3(t) \\ F_4(t) \\ F_5(t) \\ F_6(t) \\ F_7(t) \end{Bmatrix} = \begin{Bmatrix} 0 \\ 0 \\ 0 \\ c_{t4}\dot{z}_{r4} + k_{t4}z_{r4} \\ c_{t5}\dot{z}_{r5} + k_{t5}z_{r5} \\ c_{t6}\dot{z}_{r6} + k_{t6}z_{r6} \\ c_{t7}\dot{z}_{r7} + k_{t7}z_{r7} \end{Bmatrix} \tag{28}$$

Introducing the modal transformation $\boldsymbol{q} = \boldsymbol{V}\boldsymbol{Q}$, where $\boldsymbol{V}$ denotes the mass-normalized modal matrix and $\boldsymbol{Q}$ the vector of modal coordinates, the response of the system can be expressed in modal space. For the configuration corresponding to $h_G = 0.7610637953$ m, the modal matrix $\boldsymbol{V}$ reads:

$$\mathbf{V} = \begin{pmatrix} -0.019063 & -0.019063 & 0.000000 & -0.000007 & 0.000000 & 0.000008 & 0.000000 \\ 0.012616 & -0.012616 & 0.000000 & 0.000005 & 0.000000 & 0.000005 & 0.000000 \\ 0.000000 & 0.000000 & 0.027936 & 0.000000 & 0.000000 & 0.000000 & -0.000008 \\ -0.000044 & 0.000000 & 0.000023 & 0.111456 & 0.079057 & -0.008810 & 0.079057 \\ -0.000044 & 0.000000 & -0.000023 & 0.111456 & -0.079057 & -0.008810 & -0.079057 \\ 0.000000 & -0.000044 & 0.000023 & -0.008810 & -0.079057 & -0.111456 & 0.079057 \\ 0.000000 & -0.000044 & -0.000023 & -0.008810 & 0.079057 & -0.111456 & -0.079057 \end{pmatrix}$$

Thus, we obtain, after computation, for mode α:

$$\ddot{Q}_\alpha + 2\xi_\alpha\omega_\alpha\dot{Q}_\alpha + \omega_\alpha^2 Q_\alpha = \mathbb{F}_\alpha(t), \qquad \alpha = \overline{1,7} \tag{29}$$

with

$$\mathbb{F}_\alpha(t) = \sum_{k=4}^{7} v_{k\alpha}\, F_k(t), \qquad \alpha = \overline{1,7} \tag{30}$$

where $v_{k\alpha}$ is the element located at the intersection of the k-th row and the α-th column of the modal matrix $\boldsymbol{V}$, and F_k denotes the k-th component of the excitation vector $\boldsymbol{F}(\boldsymbol{t})$. The parameters ξ_α and ω_α are respectively the damping ratio and the natural angular frequency associated with mode α.

The transfer function of the system, relating the excitation to the modal response, is written :

$$H_\alpha(\omega) = \frac{1}{(\omega_\alpha^2 - \omega^2) + 2i\xi_\alpha\omega_\alpha\omega}, \qquad i = \sqrt{-1} \tag{31}$$

Hence, from (29), we have:

$$\begin{cases} Q_\alpha(\omega) = H_\alpha(\omega)\mathbb{F}_\alpha(\omega) \\ \dot{Q}_\alpha(\omega) = i\omega H_\alpha(\omega)\mathbb{F}_\alpha(\omega) \end{cases} \tag{32}$$

where $\mathbb{F}_\alpha(\omega)$ is the Fourier transform of $\mathbb{F}_\alpha(t)$

Thus, the correlation matrix of the generalized velocities is [6]:

$$R_{\dot{Q}_\alpha \dot{Q}_\beta}(0) = \int_{-\infty}^{+\infty} \left(i\omega H_\alpha(\omega)\mathbb{F}_\alpha(\omega)\right) \cdot \left(-i\omega H_\beta^*(\omega)\mathbb{F}_\beta^*(\omega)\right) d\omega \tag{33}$$

which may also be written in the form

$$R_{\dot{Q}_\alpha \dot{Q}_\beta}(0) = \int_{-\infty}^{+\infty} \frac{\omega^2 \mathbb{F}_\alpha(\omega) \cdot \mathbb{F}_\beta^*(\omega)}{[(\omega_\alpha^2 - \omega^2) + 2i\xi_\alpha\omega_\alpha\omega]\left[\left(\omega_\beta^2 - \omega^2\right) - 2i\xi_\beta\omega_\beta\omega\right]} d\omega \tag{34}$$

where (*) denotes the complex conjugate.
Finally, the autocorrelation matrix $\boldsymbol{R}_{\dot{\boldsymbol{q}}\,\dot{\boldsymbol{q}}}(\mathbf{0}) = \left[R_{\dot{q}_\alpha \dot{q}_\beta}(0)\right]$, after returning to the initial variables, is written:

$$\boldsymbol{R}_{\dot{\boldsymbol{q}}\,\dot{\boldsymbol{q}}}(\mathbf{0}) = \boldsymbol{V}\boldsymbol{R}_{\dot{\boldsymbol{Q}}\,\dot{\boldsymbol{Q}}}(0)\boldsymbol{V}^T \tag{35}$$

and, in index form,

$$R_{\dot{q}_i\,\dot{q}_i}(0) = \sum_{\alpha=1}^{7} v_{i\alpha} v_{j\alpha} R_{\dot{Q}_\alpha\,\dot{Q}_\alpha}(0) + \sum_{\substack{\alpha=1 \\ \alpha\neq\beta}}^{7}\sum_{\beta=1}^{7} v_{i\alpha} v_{j\beta} R_{\dot{Q}_\alpha\,\dot{Q}_\beta}(0), \qquad i,j = \overline{1,7} \tag{36}$$

The errors on the mean-square velocity due to the omission of the modal cross-correlations $\tilde{R}_{\dot{q}_i\,\dot{q}_i}(0) = \sum_{\alpha=1}^{7} v_{i\alpha}^2 R_{\dot{Q}_\alpha\,\dot{Q}_\alpha}(0)$ are obtained, as indicated in Long et al. [7], from:

$$\eta_i = \left|\frac{\tilde{R}_{\dot{q}_i\,\dot{q}_i}(0) - R_{\dot{q}_i\,\dot{q}_i}(0)}{R_{\dot{q}_i\,\dot{q}_i}(0)}\right| \times 100, \qquad i = \overline{1,7} \tag{37}$$

and the correlation coefficient ρ_{ij} is given by:

$$\rho_{ij} = \frac{R_{\dot{q}_i\,\dot{q}_j}(0)}{\sqrt{R_{\dot{q}_i\,\dot{q}_i}(0)\,R_{\dot{q}_j\,\dot{q}_j}(0)}}, \qquad i,j = \overline{1,7} \tag{38}$$

6.1 Case 1: stationary white noise

In this part, the contact forces between the wheels and the road are modelled by a stationary white noise of intensity S_0, applied to the front left wheel and then reproduced on the other wheels with the following time delays: $\Delta t_4 = 0$ (front left wheel), $\Delta t_5 = t_{ec}$ (front right wheel), $\Delta t_6 = t_\delta$ (rear left wheel) and $\Delta t_7 = t_{ec} + t_\delta$ (rear right wheel). Thus, the cross power spectral density (CPSD) of the excitations applied to modes α and β is:

$$\mathbb{F}_\alpha(\omega)\cdot\mathbb{F}_\beta^*(\omega)=S_0\sum_{k=4}^{7}\sum_{j=4}^{7}v_{k\alpha}v_{j\beta}\,e^{-i\omega(\Delta t_k-\Delta t_j)} \tag{39}$$

Thus, the correlation matrix of the generalized velocities $\dot{Q}_i$, is written, setting $\tau=\Delta t_k-\Delta t_j$:

$$R_{\dot{Q}_\alpha\dot{Q}_\beta}(0)=\begin{cases}S_0\left[2\sum\limits_{4\le k<j\le 7}v_{k\alpha}\,v_{j\alpha}\,G_1(\tau)+G_1(0)\sum\limits_{k=4}^{7}v_{k\alpha}^2\right], & if\ \alpha=\beta\\ S_0\left[\sum\limits_{4\le k<j\le 7}\left(v_{k\alpha}v_{j\beta}\,G_2(\tau)+v_{j\alpha}v_{k\beta}\,G_2(-\tau)\right)+G_2(0)\sum\limits_{k=4}^{7}v_{k\alpha}\,v_{k\beta}\right], & if\ \alpha\neq\beta\end{cases} \tag{40},$$

where

$$\begin{cases}G_1(\tau)=\int_{-\infty}^{+\infty}\dfrac{\omega^2e^{-i\omega\tau}}{(\omega_\alpha^2-\omega^2)^2+(2\xi_\alpha\omega_\alpha\omega)^2}d\omega\\ G_2(\tau)=\int_{-\infty}^{+\infty}\dfrac{\omega^2.e^{-i\omega\tau}}{[(\omega_\alpha^2-\omega^2)+2i\xi_\alpha\omega_\alpha\omega]\left[\left(\omega_\beta^2-\omega^2\right)-2i\xi_\beta\omega_\beta\omega\right]}d\omega\end{cases} \tag{41}$$

After computing (41) by the residue method and for every $\xi_\alpha,\xi_\beta>0$, one obtains:

$$G_2(\tau)=\frac{2\pi\,e^{-\lambda|\tau|}}{\Delta}\left[2PC_W(|\tau|)+BS_W(|\tau|)\right], \tag{42}$$

With

$$\lambda_\alpha=\xi_\alpha\omega_\alpha,\qquad W_\alpha=\omega_\alpha^2(1-\xi_\alpha^2),\qquad \lambda_\beta=\xi_\beta\omega_\beta,\qquad W_\beta=\omega_\beta^2\left(1-\xi_\beta^2\right)$$

where, for any real W and any $t\geq 0$,

$$C_W(t)=\begin{cases}\cos\left(\sqrt{W}t\right), & W>0\\ 1, & W=0\\ \cosh\left(-\sqrt{W}t\right), & W<0\end{cases},\qquad S_W(t)=\begin{cases}\dfrac{\sin\left(\sqrt{W}t\right)}{\sqrt{W}}, & W>0\\ t, & W=0\\ \dfrac{\sinh\left(\sqrt{-W}t\right)}{\sqrt{-W}}, & W<0\end{cases} \tag{43}$$

$$\Delta=\left(\omega_\alpha^2-\omega_\beta^2\right)^2+4\lambda_\alpha\lambda_\beta\left(\omega_\alpha^2+\omega_\beta^2\right)+4\left(\lambda_\alpha^2\omega_\beta^2+\lambda_\beta^2\omega_\alpha^2\right),\qquad P=\lambda_\alpha\omega_\beta^2+\lambda_\beta\omega_\alpha^2$$

- $if\ \tau\geq 0,\ \lambda=\lambda_\beta,\ W=W_\beta,\ B=\omega_\beta^2\left(\omega_\alpha^2-\omega_\beta^2\right)-2\lambda_\beta P$
- $if\ \tau\leq 0,\ \lambda=\lambda_\alpha,\ W=W_\alpha,\ B=\omega_\alpha^2\left(\omega_\beta^2-\omega_\alpha^2\right)-2\lambda_\alpha P$

and for $\alpha=\beta$, we have

$$G_1(\tau)=\frac{\pi\,e^{-\lambda_\alpha|\tau|}}{2\lambda_\alpha}\left[C_{W_\alpha}(|\tau|)-\lambda_\alpha S_{W_\alpha}(|\tau|)\right]. \tag{44}$$

We observe that, for $\tau=0$, the obtained results coincide with those of Long et al. [7] for a single applied force. Our approach nevertheless differs from their work in that it accounts for the excitations of all four wheels, rather than a single force applied to one wheel, which would introduce a double summation in computing the autocorrelation matrix.

Note: In the remainder of this section, the intensity S_0 of the stationary white noise is set to $1\ m^2.s/rad$. Since the system's response is linear with respect to the excitation, the mean-square velocities are proportional to S_0 and the root-mean-square values are proportional to $\sqrt{S_0}$.

Table 5. Comparison of the mean-square velocities obtained with the complete modal sum $R_{\dot{q}_i\,\dot{q}_i}(0)$ and by neglecting the modal cross-correlations $\tilde{R}_{\dot{q}_i\,\dot{q}_i}(0)$, together with the corresponding relative errors η_i. Results for an ideal symmetric vehicle with a single wheel excited, for $h_G = 0$ m and $h_G \approx 0.761$ m, with and without anti-roll bars.

DOF ($h_G = 0\ m$)	$k_\varphi = 0$			$k_\varphi = 62{,}085\ N.m/rad$		
	$R_{\dot{q}_i\,\dot{q}_j}(0)$	$\tilde{R}_{\dot{q}_i\,\dot{q}_i}(0)$	$\eta_i(\%)$	$R_{\dot{q}_i\,\dot{q}_j}(0)$	$\tilde{R}_{\dot{q}_i\,\dot{q}_i}(0)$	$\eta_i(\%)$
Heave z	3.6109×10^{-12}	3.6110×10^{-12}	0.00	3.6109×10^{-12}	3.6110×10^{-12}	0.00
Pitch θ	2.1195×10^{-12}	2.1195×10^{-12}	0.00	2.1195×10^{-12}	2.1195×10^{-12}	0.00
Roll φ	1.0258×10^{-11}	1.0259×10^{-11}	0.00	3.9454×10^{-11}	3.9462×10^{-11}	0.02
Wheel 1 (excited)	4.3083×10^{-7}	1.0771×10^{-7}	**75.00**	4.3013×10^{-7}	1.0753×10^{-7}	**75.00**
Wheel 2	8.4208×10^{-18}	1.0771×10^{-7}	–	5.9223×10^{-13}	1.0753×10^{-7}	–
Wheel 3	6.7545×10^{-18}	1.0771×10^{-7}	–	4.0790×10^{-16}	1.0753×10^{-7}	–
Wheel 4	2.4301×10^{-17}	1.0771×10^{-7}	–	4.1069×10^{-16}	1.0753×10^{-7}	–
DOF ($h_G = 0.761\ m$)	$k_\varphi = 0$			$k_\varphi = 62{,}085\ N.m/rad$		
	$R_{\dot{q}_i\,\dot{q}_j}(0)$	$\tilde{R}_{\dot{q}_i\,\dot{q}_i}(0)$	$\eta_i(\%)$	$R_{\dot{q}_i\,\dot{q}_j}(0)$	$\tilde{R}_{\dot{q}_i\,\dot{q}_i}(0)$	$\eta_i(\%)$
Heave z	3.6109×10^{-12}	3.6461×10^{-12}	0.97	3.6109×10^{-12}	3.6290×10^{-12}	0.50
Pitch θ	1.5816×10^{-12}	1.5662×10^{-12}	0.97	1.5816×10^{-12}	1.5737×10^{-12}	0.50
Roll φ	3.8767×10^{-12}	3.8767×10^{-12}	0.00	1.4897×10^{-11}	1.4897×10^{-11}	0.00
Wheel 1 (excited)	4.3083×10^{-7}	1.1934×10^{-7}	**72.30**	4.3013×10^{-7}	1.6135×10^{-7}	**62.49**
Wheel 2	2.1111×10^{-17}	1.1934×10^{-7}	–	5.9139×10^{-13}	1.6135×10^{-7}	–
Wheel 3	2.6637×10^{-18}	9.6080×10^{-8}	–	1.5111×10^{-16}	5.3715×10^{-8}	–
Wheel 4	2.6638×10^{-18}	9.6080×10^{-8}	–	1.5111×10^{-16}	5.3715×10^{-8}	–

Table 5 gives, for $h_G = 0$ and $h_G = \sqrt{m_c(m_c L^2 - J_{yy})}/m_c \approx 0.761\ m$, the mean-square velocity response of each degree of freedom computed with the direct modal sum, $R_{\dot{q}_i\,\dot{q}_j}(0)$, and with the modal cross-correlation terms omitted, $\tilde{R}_{\dot{q}_i\,\dot{q}_i}(0)$, together with the relative error η_i on the mean-square velocity. The dashes indicate relative errors that are not meaningful for the non-excited wheels, whose exact responses are of the order of 10^{-16} to 10^{-18}. For $h_G = 0\ m$, we obtain an error of 75% on the excited wheel, as reported by Long et al. [7], with and without anti-roll bars. For $h_G \approx 0.761\ m$, by contrast, the error due to the omission of the cross-correlations falls to 72.30% without anti-roll bars and to 62.49% with them. Heave and pitch coincide (see also Table 4), with errors of 0.97% without bars and 0.50% with bars, whereas for roll, which is decoupled from the other two body modes, the error remains zero. For the symmetric vehicle with a single wheel excited, omitting the modal cross-correlations is therefore of no consequence for the body modes (≤ 1% even at the critical heights) and affects only the excited wheel.

Two types of correlation enter the computation of the mean-square responses: the modal cross-correlations, corresponding to the terms $\alpha \neq \beta$ between different modes, and the correlations between the wheel excitations, associated with the terms $k \neq j$, since the four wheels follow the same road profile with time delays. When a single wheel is excited, only the modal cross-correlations are involved. When all four wheels are excited, both types of correlation coexist, and their omission is examined separately in Figures 6 and 7.

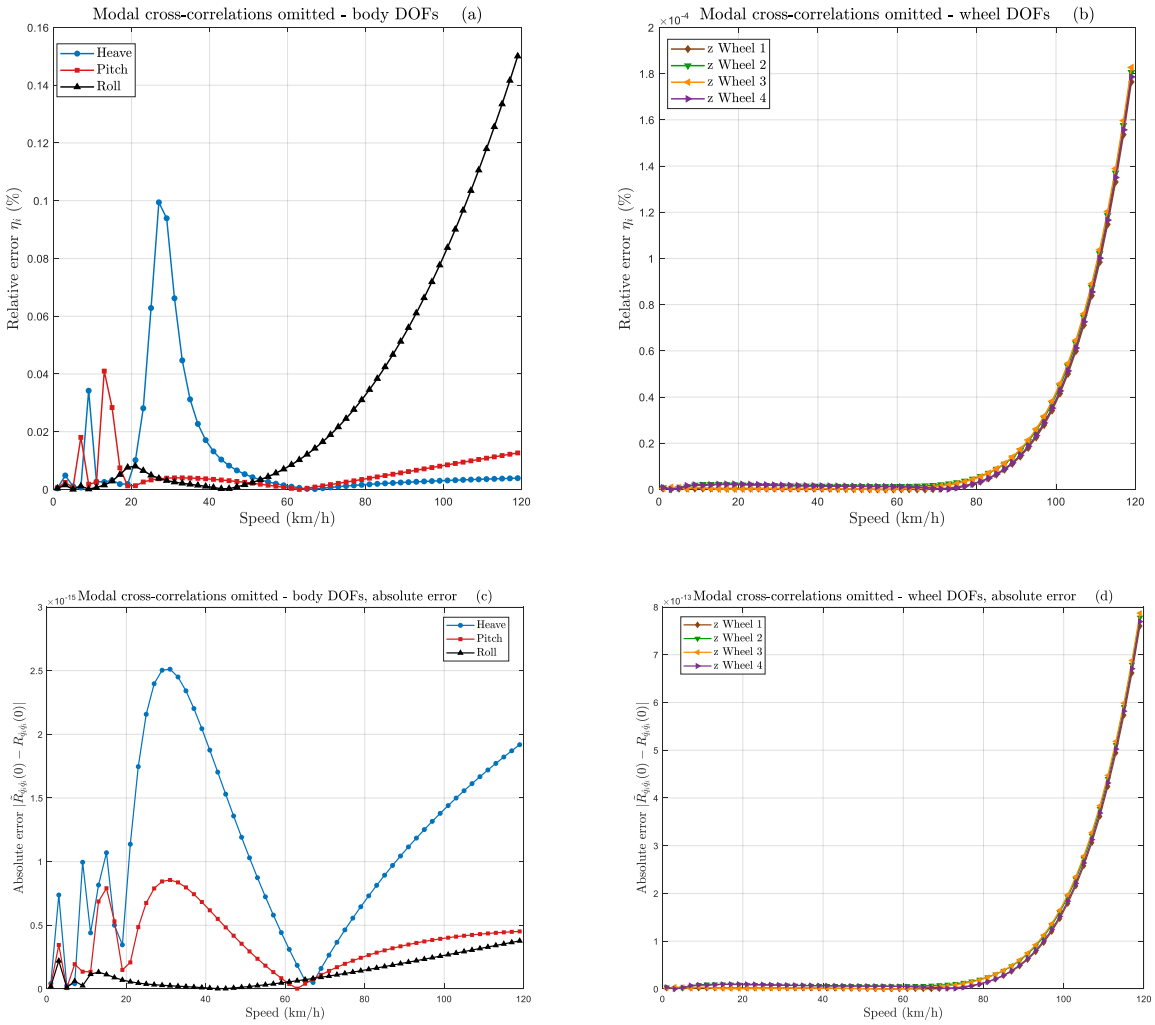


Figure 6: Omission of the modal cross-correlations ($\alpha \neq \beta$) for a symmetric vehicle without anti-roll bars, with h_G = 0.761 m, under stationary white noise applied to the four wheels with time delays: (a) relative error on $R_{\dot{q}_i\,\dot{q}_j}(0)$ for the body degrees of freedom; (b) relative error for the wheel degrees of freedom; (c) absolute error $\left|\tilde{R}_{\dot{q}_i\,\dot{q}_i}(0) - R_{\dot{q}_i\,\dot{q}_i}(0)\right|$ for the body degrees of freedom; and (d) absolute error for the wheel degrees of freedom.

When moving from single-wheel excitation (Table 5) to correlated excitation of the four wheels with delays, for h_G = 0.761 m and without anti-roll bars (Figure 6), the errors due to the omission of the modal cross-correlations are negligible for all degrees of freedom. For the body (Figure 6.a), heave shows two peaks, 0.034% at 9 km/h and 0.10% at 27 km/h, and then vanishes around 60 km/h, while pitch reaches 0.02% at 7 km/h and 0.041% at 13 km/h. Roll remains below 0.01% up to about 63 km/h and then increases to 0.15% at 120 km/h. For the wheels (Figures 6.b and 7.d), the errors are of the order of 10^{-4}% in relative terms and 10^{-13} in absolute terms, and are practically identical for the four wheels. In absolute terms (Figure 6.c), the discrepancy for the body degrees of freedom is of the order of 10^{-15}, i.e., four orders of magnitude below their mean-square values. The error nevertheless remains below 0.16% over the whole speed range considered (0 to 120 km/h), and below 0.013% for heave and pitch. This result confirms and extends that of Table 5: omitting the modal cross-correlations, which produces a 75% error on the excited wheel when a single wheel is excited, becomes inconsequential when all four wheels are

excited, because the cross terms of the four nearly degenerate wheel modes cancel out between the contact points. The correlated excitation of the four wheels thus regularizes the truncated modal sum.

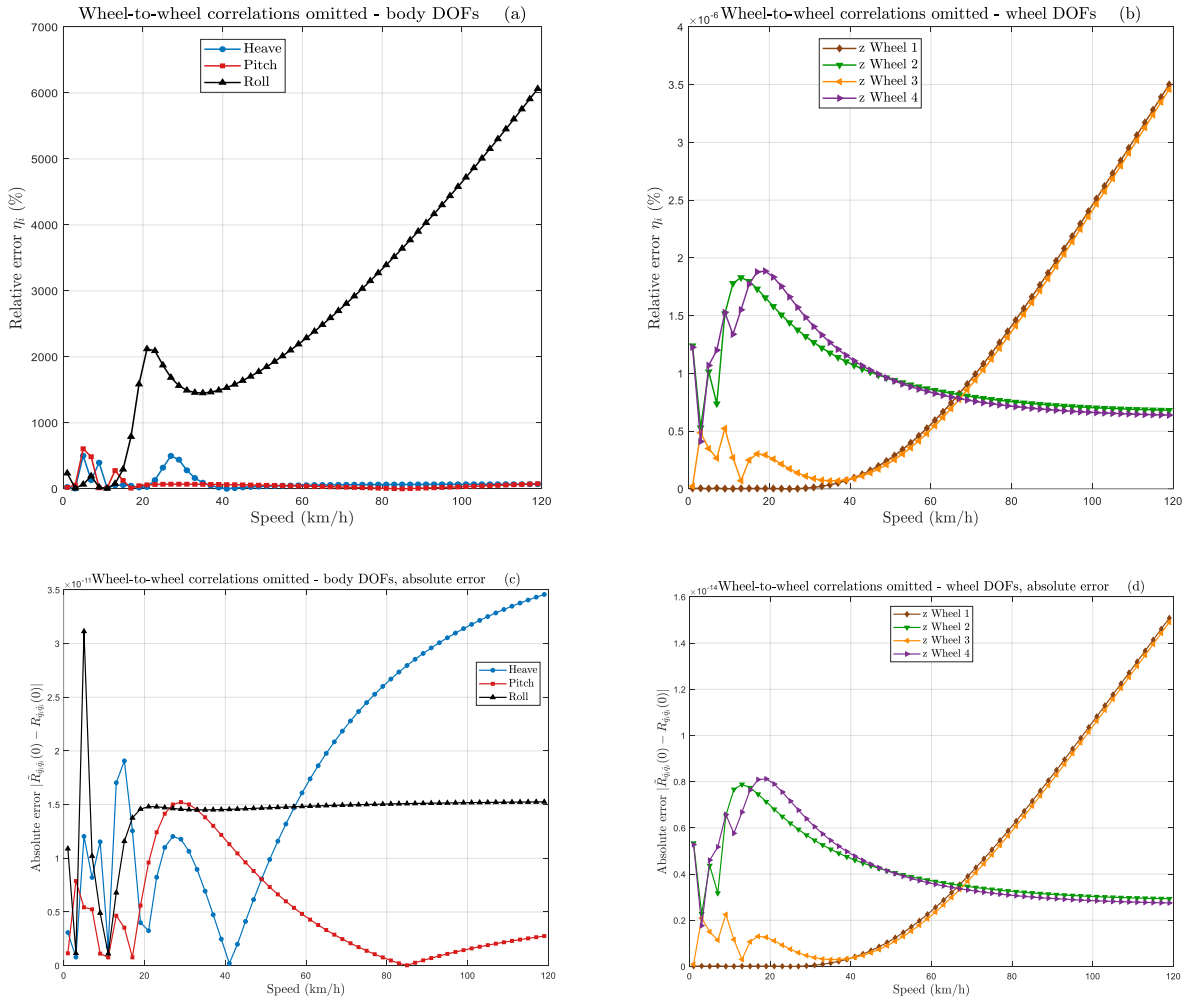


Figure 7: Omission of the correlations between the wheel excitations (k ≠ j, wheels assumed independent) for a symmetric vehicle without anti-roll bars, with $h_G = 0$, under stationary white noise applied to the four wheels with time delays: (a) relative error on $R_{\dot{q}_i\,\dot{q}_i}(0)$ for the body degrees of freedom; (b) relative error for the wheel degrees of freedom; (c) absolute error $\left|\tilde{R}_{\dot{q}_i\,\dot{q}_i}(0) - R_{\dot{q}_i\,\dot{q}_i}(0)\right|$ for the body degrees of freedom.

The omission of the correlations between the wheel excitations (k ≠ j, wheels assumed independent) for all modal terms is examined in Figure 7. The results show that this approximation can lead to significant discrepancies, underlining the essential role of the correlation terms in evaluating the vibration response of the vehicle. The roll error exceeds 2,000%, whereas the heave and pitch errors remain below 610%. The roll error (Figure 7.a) is not monotonic: it peaks at 2,130% around 21 km/h, falls back to 1,453% around 35 km/h and then rises to 6,064% at 120 km/h. Heave and pitch reach their maximum values, 501% and 607% respectively, around 5 km/h. For the wheels (Figure 7.b), the errors are of the order of 10^{-6}%. Figure 7.c shows the absolute errors of the body modes. The roll error is practically constant above 20 km/h, at about 1.5×10^{-11} rad^2/s^2. In absolute terms, heave suffers the largest error at high speed, 3.47×10^{-11} m^2/s^2 at 120 km/h. In the modal superposition, the small roll response results from a compensation

between the self-term of each wheel and the wheel-to-wheel cross terms, whose signs are opposite for the left and right wheels. Removing these terms therefore breaks the compensation and leaves a residual that depends little on speed. The two types of correlation thus carry very different weights: the modal cross-correlations can be omitted when all four wheels are excited (Figure 6), whereas the interwheel correlations can under no circumstances be omitted, especially for roll (Figure 7.a). Omitting the interwheel correlations would amount to computing the response of a vehicle whose four wheels run on four different, unrelated roads. In a real vehicle, the left and right wheels of the same axle encounter the same profile up to a lateral offset, and the rear axle encounters what the front axle encountered $(L_1 + L_2)/v$ seconds earlier.

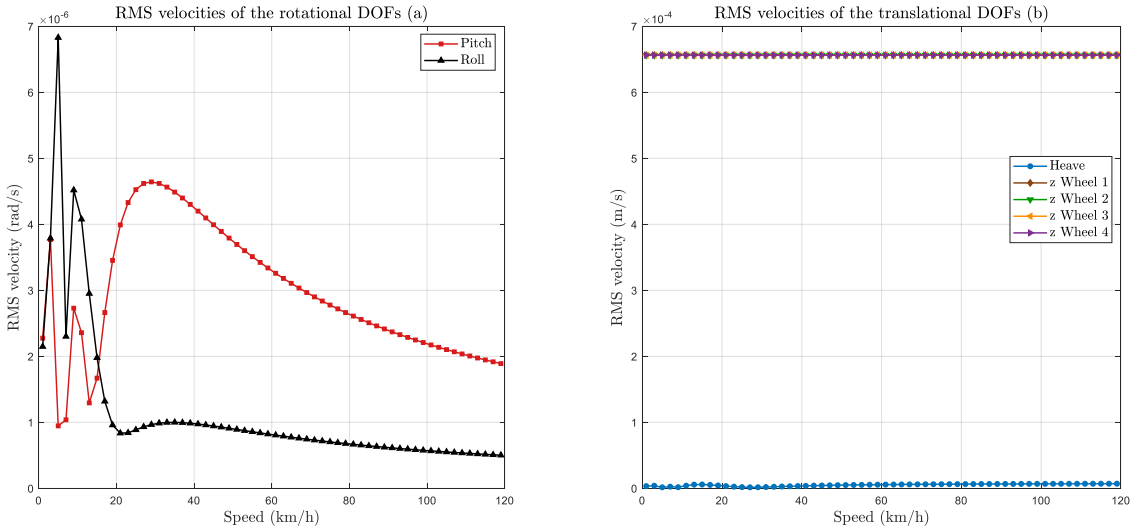


Figure 8: RMS values of the generalized velocities of the rotational (a) and translational (b) degrees of freedom as functions of vehicle speed, for stationary white noise.

The RMS values of the generalized velocities under stationary white-noise excitation are shown in Figure 8 as functions of vehicle speed. The RMS values of the four vertical wheel displacements are independent of speed: they equal 6.56×10^{-4} m/s for both the front and rear wheels over the whole range considered (Figure 8.b). This behavior is consistent with the nature of the excitation. Since the white-noise spectral density is constant, speed enters only through the delays between the contact points, which affect only the cross terms and not the dominant diagonal terms of the wheel modes. The RMS value of heave, by contrast, is much smaller and varies little: over the whole range it remains about one hundred times lower than the wheel RMS values, at 5.5×10^{-6} m/s on average. The rotational degrees of freedom, shown in Figure 8.a, both decrease monotonically above 30 km/h after reaching maxima at low speeds: 4.65×10^{-6} rad/s at 29 km/h for pitch and 6.83×10^{-6} rad/s at 5 km/h for roll. This decrease reflects the fact that, as vehicle speed increases, the delays between axles become shorter and the four excitations become more alike, which favors heave at the expense of pitch and roll. The small mean-square value of the roll velocity explains the magnitude of the relative errors in Figure 7.a. For comfort, the critical speeds under white noise are therefore the low speeds, not the high speeds at which the four excitations become alike and only heave remains.

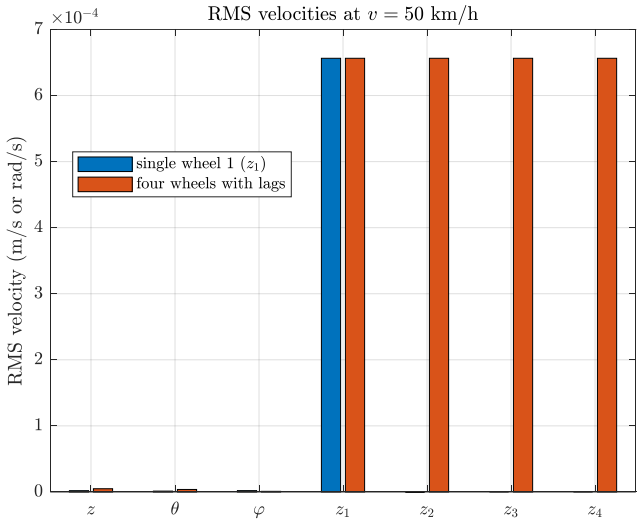


Figure 9: RMS values of the generalized velocities at 50 km/h: single-wheel excitation (blue) and excitation of the four wheels with delays (red), white-noise case.

Figure 9 compares, at 50 km/h, the RMS values of the seven degrees of freedom for single-wheel excitation and for excitation of the four wheels with delays. With a single wheel excited, only that wheel responds, at 6.56×10^{-4} m/s, whereas with four wheels excited each wheel responds at the same level, so that the energy injected into the vehicle is four times greater. The RMS value of the excited wheel is the same in both cases, which shows that the interwheel delays do not affect the individual mean-square velocities of the unsprung masses. The body responses are invisible at this scale in both configurations. The configuration of Long et al. [7] therefore underestimates the total vibrational energy by a factor of four and concentrates the response on a single wheel; it is this concentration, not the response level, that governs the 75% error it reveals.

Figures 10 and 11 show side by side, in discrete form, the coefficients of the autocorrelation matrix and the correlation coefficients of the physical degrees of freedom, for single-wheel excitation and for excitation of the four wheels with delays. A color-map representation, commonly used for modal comparison matrices [32], provides an overall view.

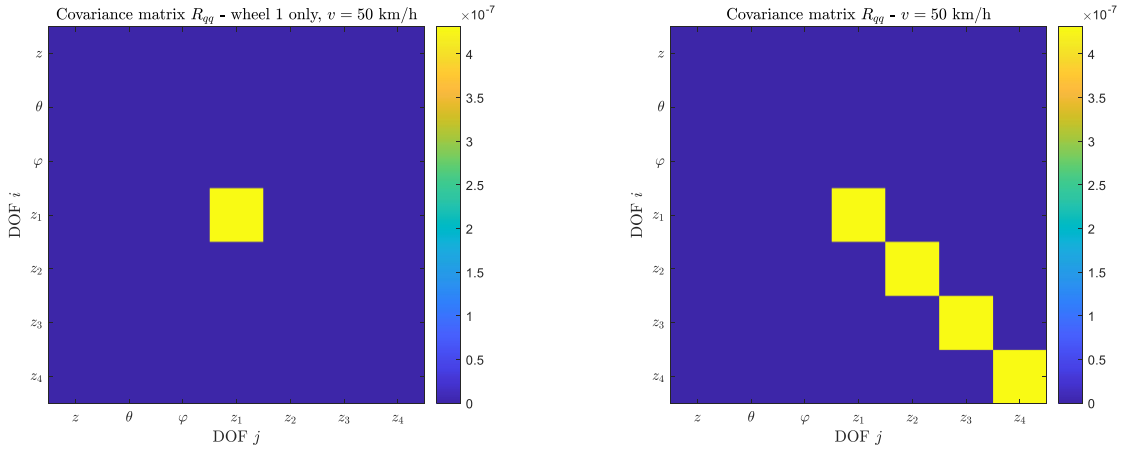


Figure 10: Color map of the autocorrelation matrix $R_{\dot{q}_i \dot{q}_i}(0)$ at 50 km/h for stationary white noise: (a) single wheel excited (z_1); (b) four wheels excited with delays.

Figure 10 shows the autocorrelation matrix of the generalized velocities at 50 km/h. Its diagonal terms, which correspond to the mean-square velocities, largely dominate the off-diagonal terms. With a single wheel excited (Figure 10.a), only the front left wheel (wheel 1) responds, at 4.3083×10^{-7} m^2/s^2, whereas with four wheels excited (Figure 10.b) each wheel shows this same value, confirming the previous results. Heave, pitch and roll remain much smaller and do not appear at this scale. The off-diagonal terms remain small compared with the diagonal terms. The residual correlations arise because the four wheels are not subjected to independent excitations but to one and the same excitation, delayed according to their position on the vehicle.

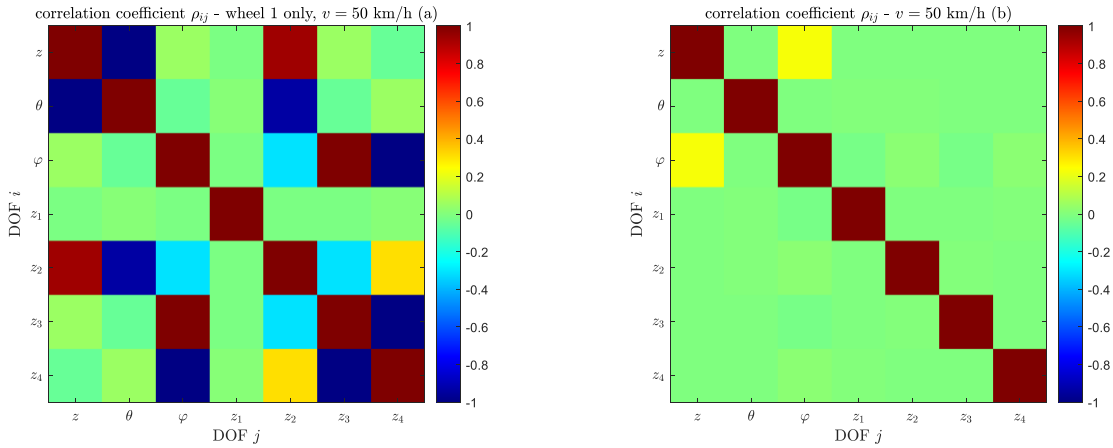


Figure 11: Correlation coefficient ρ_{ij} of the vehicle degrees of freedom at 50 km/h for stationary white noise: (a) single wheel excited (z_1); (b) four wheels excited with delays.

Figure 11 shows the correlation coefficient ρ_{ij}, which measures the spatial coupling between two physical degrees of freedom, at 50 km/h for stationary white noise. With a single wheel excited (Figure 11.a), wheel z_1 is uncorrelated with all other degrees of freedom, but the residual responses of the other degrees of freedom are fully correlated with one another, with coefficients close to 1 in absolute value. These extreme values reflect the fact that, under a single excitation, the small responses of the non-excited degrees of freedom are all driven by the same signal transmitted through the structure and are therefore proportional to one another, up to a sign. With the four wheels excited (Figure 11.b), all off-diagonal terms remain below 0.10 in absolute value, except for the heave–roll coupling, which is close to 0.2. The vehicle degrees of freedom can therefore be regarded as practically uncorrelated. This result must not be confused with those of Figures 6 and 7. The low coefficients observed here concern the spatial coupling, i.e., the correlation between the responses of two physical degrees of freedom, whereas the errors in Figures 6 and 7 concern the cross terms between modes ($\alpha \neq \beta$) or between wheels ($k \neq j$) in the computation of each diagonal term. Nearly uncorrelated degrees of freedom therefore by no means imply that the interwheel correlations are negligible: their omission produces errors of more than 1,800% in roll, 40% in heave and 50% in pitch at 50 km/h (Figure 7.a), whereas the largest correlation coefficient does not exceed 0.2.

6.2 Case 2: Speed-bump crossing

In this part, the obstacle is represented by the speed bump given by equation (17). Wheels k and j belonging to different axles never engage the obstacle simultaneously. The vehicle considered is symmetric. l_b and h_0 denotes the half-width and the height of the speed bump, respectively.
Unlike the stationary white-noise case, the speed-bump crossing is a deterministic transient event: the excitation acts only once, over the finite time interval $T = t_2 - t_1$ (t_1 and t_2 are the starting and ending times of the speed bump, respectively). Ensemble averages and power spectral densities are therefore not defined here. The quantity to be computed in this case is thus the time-integrated product of the modal velocities, which follows from Parseval's theorem. The distinction between power and energy spectral densities for transient signals, together with the corresponding form of Parseval's identity, is discussed in detail in [33,34]. Here the autocorrelation is understood in its deterministic sense, as the time integral of the product of two finite-energy signals rather than as an ensemble average; its value at zero time lag is accordingly expressed in m²/s:

$$E_{\dot{Q}_\alpha \dot{Q}_\beta} = \frac{1}{2\pi}\int_{-\infty}^{+\infty} \left(i\omega H_\alpha(\omega)\mathbb{F}_\alpha(\omega)\right)\cdot\left(-i\omega H_\beta^*(\omega)\mathbb{F}_\beta^*(\omega)\right) d\omega \tag{45}$$

The cross-energy spectral density of the excitations applied to modes α and β is:

$$\mathbb{F}_\alpha(\omega)\cdot\mathbb{F}_\beta^*(\omega) = \left(\sum_{k=4}^{7} v_{k\alpha}\left(k_{tk}z_{rk}(\omega) + c_{tk}\dot{z}_{rk}(\omega)\right)\right)\left(\sum_{j=4}^{7} v_{j\beta}\left(k_{tj}z_{rj}^*(\omega) + c_{tj}\dot{z}_{rj}^*(\omega)\right)\right)$$

From the road profile (equation 17), the Fourier transform of $z_{r1}(t)$ is obtained in the form:

$$z_{r1}(\omega) = z_0(\omega)\cdot e^{-i\omega\left(\frac{t_1+t_2}{2}\right)} \quad \text{and} \quad z_0(\omega) = \frac{h_0 \sin\left(\frac{\omega l_b}{2v}\right)}{\omega\left[1-\left(\frac{\omega l_b}{2\pi v}\right)^2\right]}$$

For wheel k we have the following relations:

$$\begin{cases} z_{rk}(\omega) = z_{r1}(\omega)\cdot e^{-i\omega\Delta t_k} \\ \dot{z}_{rk}(\omega) = i\omega z_{r1}(\omega)\cdot e^{-i\omega\Delta t_k} \end{cases} \tag{46}$$

hence

$$F_k(\omega) = (k_{tk} + i\omega c_{tk})\cdot z_0(\omega)\cdot e^{-i\omega\left(\frac{t_1+t_2}{2}\right)}\cdot e^{-i\omega\Delta t_k}$$

Consequently, we obtain:

$$\mathbb{F}_\alpha(\omega)\cdot\mathbb{F}_\beta^*(\omega) = |z_0(\omega)|^2\left(\sum_{k=4}^{7} v_{k\alpha}\left(k_{tk} + i\omega c_{tk}\right)\cdot e^{-i\omega\Delta t_k}\right)\left(\sum_{j=4}^{7} v_{j\beta}\left(k_{tj} - i\omega c_{tj}\right)\cdot e^{i\omega\Delta t_j}\right)$$

which gives, for $k_{tk} = k_{tj} = k_t$ and $c_{tk} = c_{tj} = c_t$

$$\mathbb{F}_\alpha(\omega)\cdot\mathbb{F}_\beta^*(\omega) = |z_0(\omega)|^2|K(\omega)|^2\sum_{k=4}^{7}\sum_{j=4}^{7} v_{k\alpha}v_{j\beta}.e^{-i\omega(\Delta t_k - \Delta t_j)} \tag{47}$$

Here $|K(\omega)|^2 = k_t^2 + \omega^2 c_t^2$.

Finally, from (45), the autocorrelation matrix of the generalized velocities for the speed-bump crossing is written:

$$E_{\dot{Q}_\alpha \dot{Q}_\beta} = \begin{cases} \dfrac{1}{\pi} \displaystyle\sum_{4 \le k < j \le 7} v_{k\alpha}\, v_{j\alpha}\, J_1(\tau) + \dfrac{J_1(0)}{2\pi} \sum_{k=4}^{7} v_{k\alpha}^2\,, & \text{if } \alpha = \beta \\ \dfrac{1}{2\pi} \displaystyle\sum_{4 \le k < j \le 7} \left(v_{k\alpha} v_{j\beta}\, J_2(\tau) + v_{j\alpha} v_{k\beta}\, J_2(-\tau) \right) + \dfrac{J_2(0)}{2\pi} \sum_{k=4}^{7} v_{k\alpha}\, v_{k\beta}, & \text{if } \alpha \neq \beta \end{cases} \tag{48}$$

where

$$\begin{cases} J_1(\tau) = \displaystyle\int_{-\infty}^{+\infty} \frac{\omega^2 |z_0(\omega)|^2 |K(\omega)|^2 . e^{-i\omega\tau}}{(\omega_\alpha^2 - \omega^2)^2 + (2\xi_\alpha \omega_\alpha \omega)^2} d\omega \\ J_2(\tau) = \displaystyle\int_{-\infty}^{+\infty} \frac{\omega^2 |z_0(\omega)|^2 |K(\omega)|^2 . e^{-i\omega\tau}}{[(\omega_\alpha^2 - \omega^2) + 2i\xi_\alpha \omega_\alpha \omega]\left[\left(\omega_\beta^2 - \omega^2\right) - 2i\xi_\beta \omega_\beta \omega\right]} d\omega \end{cases} \tag{49}$$

The calculation of these two integrals (J_1 and J_2) is given in the Appendix. We now consider a speed bump of height and width $h_0 = 10\ cm$ and $l_b = 100\ cm$ respectively, that is, an aspect ratio $h_0/l_b = 1/10$. This value corresponds to the reference configuration proposed by Danho et al. [1], who showed that the amplification of the ν vehicle's vibrational responses increases as soon as this ratio exceeds 1/10, and that a speed of 50 km/h then constitutes a threshold beyond which this amplification becomes critical. Adopting this value, therefore, makes it possible to assess the effect of the cross-correlations in a limiting configuration, prior to any geometric amplification.

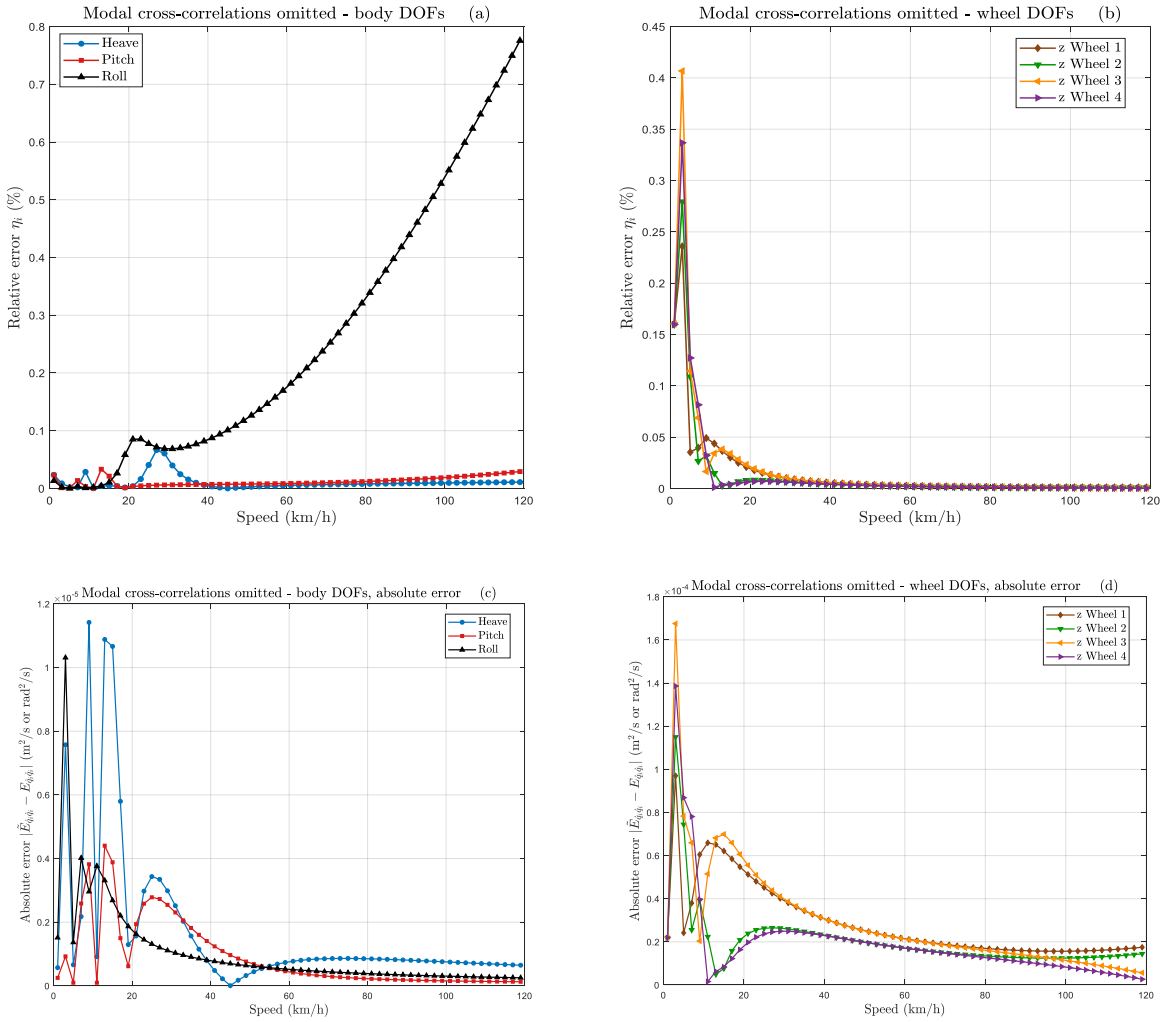


Figure 12: Speed bump: omission of the modal cross-correlations ($\alpha \neq \beta$), four wheels excited with delays, symmetric vehicle without anti-roll bars, h_G = 0.761 m: (a) relative error on $E_{\dot{q}_i\,\dot{q}_i}$ for the body degrees of freedom; (b) relative error for the wheel degrees of freedom; (c) absolute error for the body degrees of freedom; and (d) absolute error for the unsprung-mass degrees of freedom.

As can be seen in Figure 12, the error due to the omission of the modal cross-correlations also remains small for the hump-type speed bump. For the vehicle body, however, these errors are five to ten times larger than under white noise. They nevertheless remain below 0.8% over the whole speed range, roll being the only degree of freedom that is sensitive above 40 km/h (Figure 12.a). The difference from white noise lies in the transient nature of the excitation. Its spectrum, concentrated around the speed-bump angular frequency $\Omega = 2\pi v/l_b$, sweeps through the band of the body modes between 5 and 50 km/h, which reduces the compensation between body modes and wheel modes. The wheels (Figures 12.b and 13.d) are affected only at very low speeds, when the crossing duration $T = l_b/v$ becomes long compared with the period of the wheel mode. In absolute terms (Figure 12.c), the discrepancies remain three to four orders of magnitude below the body energies. The white-noise conclusion is thus confirmed for an obstacle: when all four wheels are excited, modal truncation has no effect on the results.

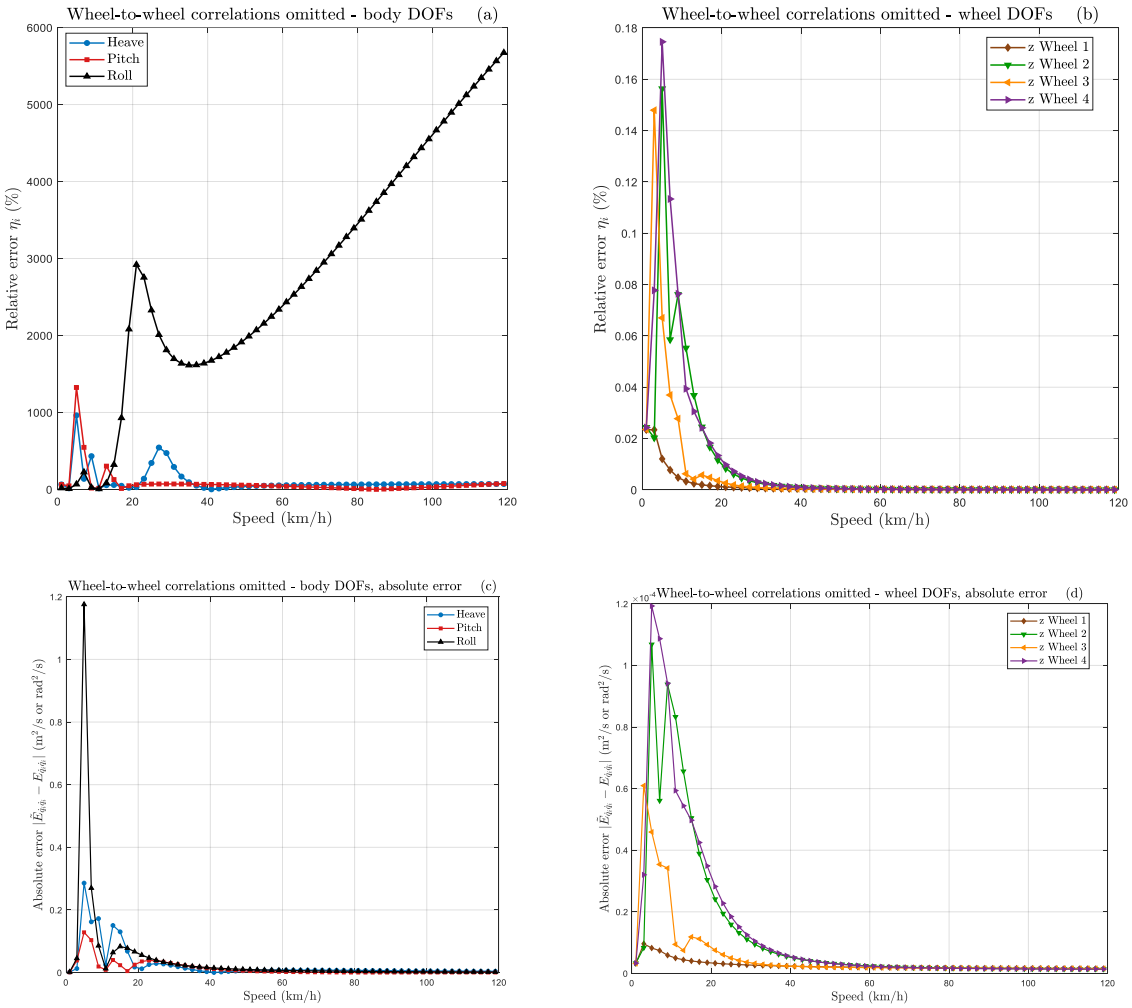


Figure 13: Speed bump: omission of the interwheel correlations (k ≠ j, wheels assumed independent), four wheels excited with delays, symmetric vehicle without anti-roll bars, h_G = 0.761 m: (a) relative error on $E_{\dot{q}_i\,\dot{q}_i}$ for the body degrees of freedom; (b) relative error for the wheel degrees of freedom; (c) absolute error for the body degrees of freedom.

The omission of the interwheel correlations (Figure 13), by contrast, remains unacceptable, especially at low speeds. Roll peaks at 2,920% around 21 km/h and exceeds 5,600% at 120 km/h. Heave and pitch reach 1,000% and 1,320% around 5 km/h before falling below 100% above 40 km/h (Figure 13.a). Under white noise (Figure 7.a), the relative roll error was large because the exact mean-square roll velocity, in the denominator of η_i, was itself very small. This is no longer the case for the speed bump: at 5 km/h, the discrepancy reaches 1.18 rad²/s in roll, 0.29 m²/s in heave and 0.13 rad²/s in pitch (Figure 13.c). The interpretation is the same as for Figure 7. The two wheels of the same axle cross the obstacle at very close instants, so that the roll motion of the body arises solely from the lateral offset between the left and right wheels. The rear axle then crosses the same obstacle with a delay $(L_1 + L_2)/v$. The independent-wheel assumption removes both of these links: the excitations of the four wheels become four unrelated events, which generates a roll motion with no physical existence and destroys the ordered succession of the two pulses that governs pitch. A model based on this assumption would overestimate the roll loading when crossing speed bumps, and hence the required roll stiffness, while failing to reproduce the crossing speeds that are most unfavorable for comfort.

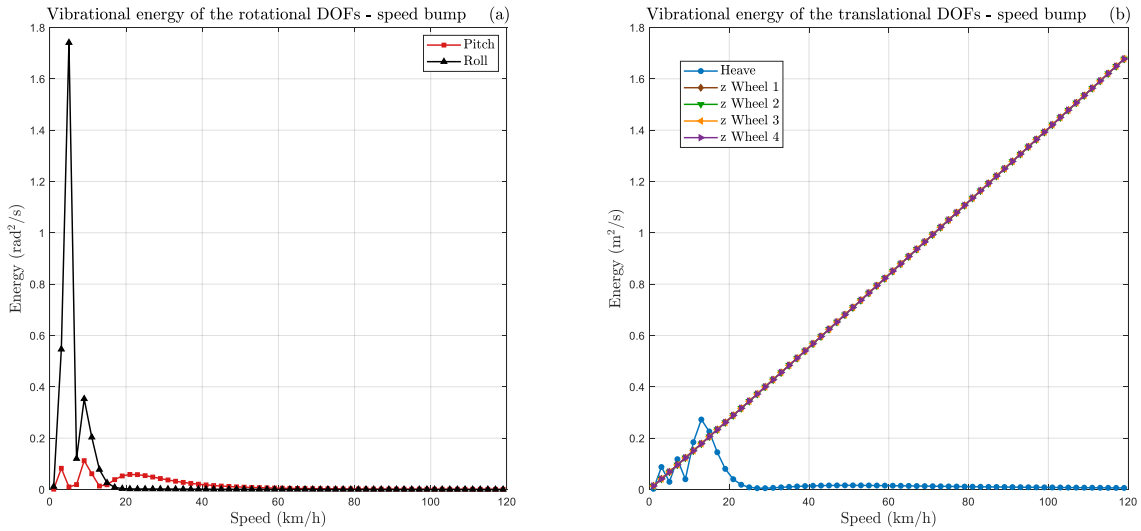


Figure 14: Speed bump: vibrational energies $E_{\dot{q}_i\, \dot{q}_i}$ of the rotational (a) and translational (b) degrees of freedom as functions of vehicle speed, four wheels excited with delays.

Figure 14 highlights the essential differences between crossing an obstacle and driving on a random road. The wheel energy increases linearly with speed, from zero to 1.68 m²/s at 120 km/h. Since the vehicle moves in a straight line, the vertical velocity imposed on the vehicle, and hence on the wheels, is proportional to the factor $h_0^2\Omega^4$ (Eq. A2), and therefore to l_b/v. The shorter the crossing, the larger the vertical impulse transmitted to the wheel. The body, by contrast, receives energy only at low speeds. Heave reaches 0.28 m²/s around 13 km/h, pitch 0.10 rad²/s around 8 km/h and roll 1.75 rad²/s at 5 km/h, i.e., seventeen times the maximum pitch value; this last maximum corresponds to the speed at which the lateral offset l_{ec}/v between the left and right wheels equals half a roll period. Above 30 km/h, the body response becomes negligible and the energy supplied by the speed bump is almost entirely absorbed by the unsprung masses. Two consequences follow. For the aspect ratio of 1/10, the critical range for comfort lies between 5 and 30 km/h, i.e., below the 50 km/h threshold established by Danho et al. [1]. Moreover, the critical speeds depend on the indicator considered: the body energy is maximal between 5 and 15 km/h, whereas the relative truncation error is maximal at 21 km/h and again above 100 km/h. The former measures the transfer of energy from the obstacle to the modes; the latter measures the weight of the cross terms relative to the diagonal terms, which is greatest when the diagonal terms become small.

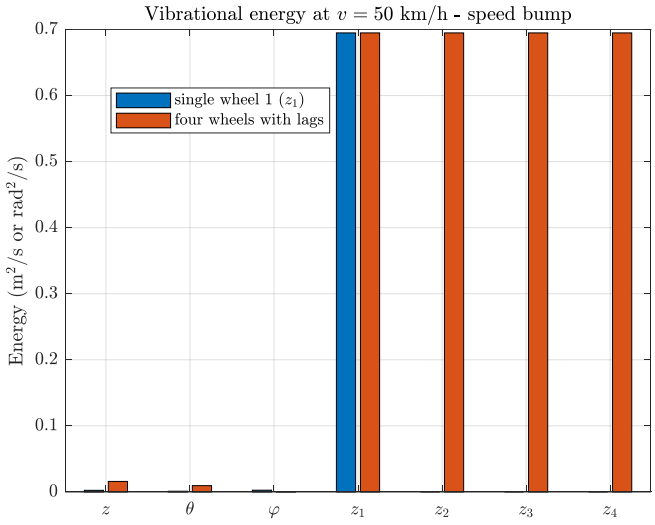


Figure 15: Vibrational energies of the seven degrees of freedom at 50 km/h, single-wheel excitation (blue) and excitation of the four wheels with delays (red), speed-bump case.

Figure 15 confirms, for the obstacle, the result obtained for white noise (Figure 9). The energy per wheel, 0.69 m^2/s at 50 km/h, is the same whether one wheel or all four are excited, and the total energy transmitted to the vehicle is four times greater in the second case. It should also be noted that, for the speed bump, unlike for white noise, heave and pitch retain non-negligible energies: 0.02 m^2/s for heave and 0.01 rad^2/s for pitch.

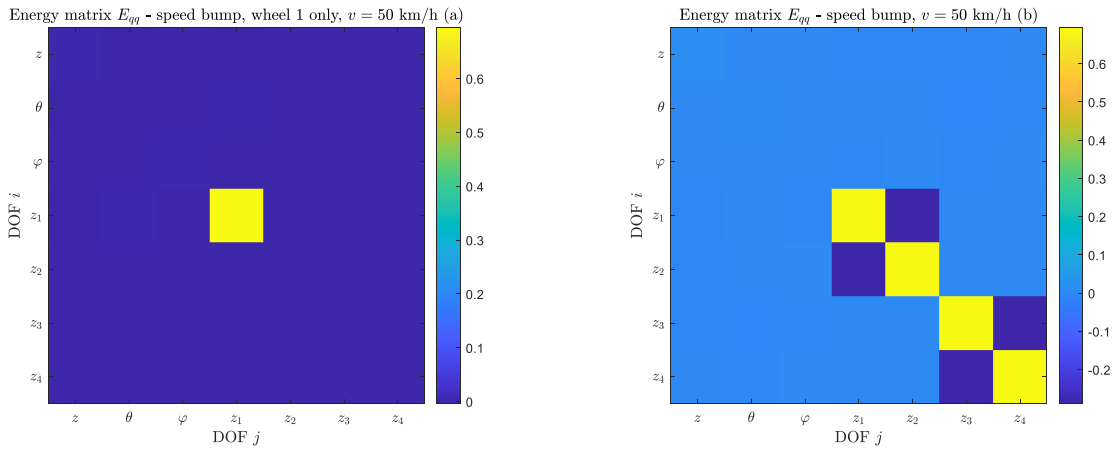


Figure 16: Color map of the energy matrix $E_{\dot{q}_i \dot{q}_i}$ at 50 km/h: (a) single wheel excited (z_1); (b) four wheels excited with delays, speed-bump case.

Figure 16 reveals a feature absent from the white-noise case. When the four wheels are excited (Figure 16.b), the cross terms between the two wheels of the same axle (z_1–z_2 and z_3–z_4) are negative, at about -0.3 m^2/s. This is because, at 50 km/h, the lateral offset l_{ec}/v = 0.043 s is of the same order as the crossing duration T = l_b/v = 0.036 s, so that the velocities of the two wheels of an axle are partly out of phase while the obstacle is being crossed. The terms between axles remain small, since the delay $(L_1 + L_2)/v$ = 0.21 s is large compared with T.

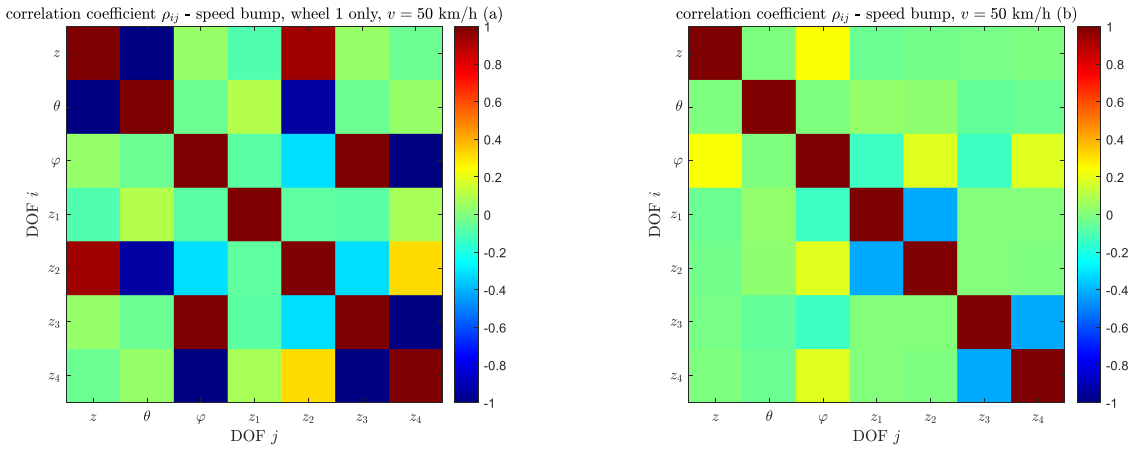


Figure 17: Correlation coefficient ρ_{ij} of the physical degrees of freedom at 50 km/h: (a) single wheel excited (z_1); (b) four wheels excited with delays, speed-bump case.

Figure 17 shows the correlation coefficients of the vehicle degrees of freedom at 50 km/h for a single wheel excited and for four wheels excited with delays, in the speed-bump case. For a single wheel excited (Figure 17.a), the previous results are recovered (Figure 11.a). For four wheels (Figure 17.b), the spatial coupling is stronger than under white noise. The wheels of the same axle are anticorrelated, with a coefficient of -0.4 reflecting the negative cross energy in Figure 16.b, and roll is correlated with the four wheels with coefficients of ± 0.3 whose sign depends on the side. A localized obstacle therefore induces a genuine spatial correlation between the body and the wheels, as well as between the wheels of the same axle. The remark made about Figure 11 still holds: a spatial correlation coefficient of at most 0.4 coexists with an error exceeding 1950% (at v = 50 km/h) when the interwheel correlations are omitted (Figure 13.a), since these two quantities do not measure the same thing.

7. Conclusion

This work has addressed the random vibration analysis of a seven-degree-of-freedom full vehicle model with repeated or closely spaced natural frequencies. A complete analytical formulation of the squares of the seven natural frequencies has been established, including the stiffness of the anti-roll bars. It reproduces the four identical wheel frequencies of Long et al. [7] in the absence of anti-roll bars and with the origin of the reference frame at the center of the sprung mass. It also provides closed-form expressions for the critical heights of the center of gravity. For the symmetric vehicle studied, with the known characteristics given above, the heave and pitch frequencies coincide at a critical height of 0.761 m, whatever the bar stiffness. The heave and roll frequencies coincide at critical heights of 0.408 m without anti-roll bars and 1.280 m with them. For the asymmetric vehicle, heave–pitch coupling prevents any coincidence between these two modes, but the roll frequency coincides with a body mode at critical heights of 0.356 m and 0.522 m without bars, and 1.089 m with bars.

The autocorrelation matrix of the generalized velocities has been obtained by the residue method for two distinct excitations. Accounting simultaneously for the four wheel contact points, rather than for a single force applied to one wheel as in Long et al. [7], introduces a double sum over the wheel pairs k and j, each pair (k, j) entering only through the delay τ_{kj} with which wheel j encounters the profile already encountered by wheel k.

For zero delay, the expressions obtained coincide with those of the literature, and the 75% error on the excited wheel reported in [7] is recovered exactly. This error stems from the omission of the cross-correlations between modes in the single-wheel configuration. It reduces to a few tenths of a percent on the body at the critical heights and vanishes as soon as the four wheels are excited with their delays, under both white noise and the speed bump, over the whole range from 1 to 120 km/h. By contrast, omitting the

correlations between the wheel excitations, which amounts to subjecting the four wheels to unrelated excitations, is acceptable in neither case. It produces a roll motion with no physical reality, with errors of 1,453 to 6,064%, and suppresses the interference between axles on which pitch depends. The main risk is therefore not neglecting the correlations between modes, but neglecting the correlations between the wheel excitations, which would lead to overestimating the required roll stiffness and to missing the speeds that are most unfavorable for comfort.

Extending the computation to low speeds reveals the critical range of the vehicle: between 5 and 30 km/h, the delays between axles and between sides equal half a pitch or roll period, and the body response is maximal for both excitations. The energy analysis of the speed bump distinguishes several critical speeds: for the aspect ratio of 1/10, the body energy is maximal between 5 and 15 km/h, below the 50 km/h threshold established by Danho et al. [1], whereas the truncation error is maximal at 21 km/h and again above 100 km/h, and the wheel energy increases linearly with speed; maximum loading and maximum error do not occur at the same speeds. Crossing an obstacle also induces a negative cross energy and an anticorrelation between the wheels of the same axle, which are absent under white noise.

Anti-roll bars, which are standard on passenger cars, must be included in the model, since they shift the coincidences involving roll, halve the effect of the heave–pitch coincidence on the body and couple the wheels of the same axle.

Appendix A: Evaluation of the integrals $J_1(\tau)$ and $J_2(\tau)$ by residue method

$$\begin{cases} J_1(\tau) = \int_{-\infty}^{+\infty} \dfrac{\omega^2 |z_0(\omega)|^2 |K(\omega)|^2 . e^{-i\omega\tau}}{(\omega_\alpha^2 - \omega^2)^2 + (2\xi_\alpha \omega_\alpha \omega)^2} d\omega \\ J_2(\tau) = \int_{-\infty}^{+\infty} \dfrac{\omega^2 |z_0(\omega)|^2 |K(\omega)|^2 . e^{-i\omega\tau}}{[(\omega_\alpha^2 - \omega^2) + 2i\xi_\alpha \omega_\alpha \omega]\left[\left(\omega_\beta^2 - \omega^2\right) - 2i\xi_\beta \omega_\beta \omega\right]} d\omega \end{cases} \quad \text{(A.1)}$$

by setting

$$T = t_2 - t_1 = \frac{l_b}{v}, \quad \Omega = \frac{2\pi v}{l_b} = \frac{2\pi}{T},$$

and

$$|Z_0(\omega)|^2 = \frac{h_0^2 \, \Omega^4 \sin^2(\omega T/2)}{\omega^2 (\Omega^2 - \omega^2)^2}, \quad |K(\omega)|^2 = k_t^2 + \omega^2 c_t^2$$

we have

$$\begin{cases} J_1(\tau) = h_0^2 \Omega^4 \int_{-\infty}^{+\infty} \dfrac{sin^2(\omega T/2)(k_t^2 + \omega^2 c_t^2) . e^{-i\omega\tau}}{(\Omega^2 - \omega^2)^2 [(\omega_\alpha^2 - \omega^2)^2 + (2\xi_\alpha \omega_\alpha \omega)^2]} d\omega \\ J_2(\tau) = h_0^2 \Omega^4 \int_{-\infty}^{+\infty} \dfrac{sin^2(\omega T/2)(k_t^2 + \omega^2 c_t^2) e^{-i\omega\tau}}{(\Omega^2 - \omega^2)^2 [(\omega_\alpha^2 - \omega^2) + 2i\xi_\alpha \omega_\alpha \omega]\left[\left(\omega_\beta^2 - \omega^2\right) - 2i\xi_\beta \omega_\beta \omega\right]} d\omega \end{cases} \quad \text{(A.2)}$$

we also have,

$$sin^2\left(\frac{\omega T}{2}\right) = \frac{1}{2} - \frac{1}{4} e^{i\omega T} - \frac{1}{4} e^{-i\omega T} \quad \text{or} \quad sin^2\left(\frac{\omega T}{2}\right) = \frac{1}{2} - \frac{1}{2}\cos(\omega T)$$

hence

$$\begin{cases} J_1(\tau) = h_0^2 \, \Omega^4 \left[\frac{1}{2} I_1(\tau) - \frac{1}{4} I_1(\tau - T) - \frac{1}{4} I_1(\tau + T)\right]. \\ J_2(\tau) = h_0^2 \Omega^4 \left[\frac{1}{2} \, I_2(\tau) - \frac{1}{4} \, I_2(\tau - T) - \frac{1}{4} \, I_2(\tau + T)\right] \end{cases} \quad \text{(A.3)}$$

with

$$\begin{cases} I_1(u) = \int_C \dfrac{(k_t^2 + \omega^2 c_t^2) e^{-i\omega u}}{(\Omega^2 - \omega^2)^2 [(\omega_\alpha^2 - \omega^2) + 2i\xi_\alpha\omega_\alpha\omega][(\omega_\alpha^2 - \omega^2) - 2i\xi_\alpha\omega_\alpha\omega]} d\omega \\ I_2(u) = \int_C \dfrac{(k_t^2 + \omega^2 c_t^2) e^{-i\omega u}}{(\Omega^2 - \omega^2)^2 [(\omega_\alpha^2 - \omega^2) + 2i\xi_\alpha\omega_\alpha\omega]\left[\left(\omega_\beta^2 - \omega^2\right) - 2i\xi_\beta\omega_\beta\omega\right]} d\omega \end{cases} \tag{A.4}$$

Here C denotes the real axis indented below $\omega = \pm\Omega$, where the splitting of the squared sine, by removing its double zero, has created double poles. Their contributions cancel in the combination (A.3), so the result is independent of the indentation. After computation in Matlab, using the residue method, one obtains:

$$I_2(u) = \begin{cases} \dfrac{2\pi\, e^{-\lambda_\beta u}}{\Theta_\beta^2\, \Delta}\left[X_\beta S_{W_\beta}(u) - \tilde{Y}_\beta C_{W_\beta}(u)\right], & u \geq 0, \\ \dfrac{2\pi\, e^{-\lambda_\alpha |u|}}{\Theta_\alpha^2\, \Delta}\left[\tilde{Y}_\alpha C_{W_\alpha}(|u|) + X_\alpha S_{W_\alpha}(|u|)\right] + I_\Omega, & u < 0. \end{cases} \tag{A.5}$$

Here Δ is the denominator of G_2 defined in the main text,

$$\Delta = \left(\omega_\alpha^2 - \omega_\beta^2\right)^2 + 4\lambda_\alpha\lambda_\beta\left(\omega_\alpha^2 + \omega_\beta^2\right) + 4\left(\lambda_\alpha^2\omega_\beta^2 + \lambda_\beta^2\omega_\alpha^2\right),$$

with $\lambda_\alpha = \xi_\alpha\omega_\alpha$ and $W_\alpha = \omega_\alpha^2(1 - \xi_\alpha^2)$; C_W and S_W are the functions defined in Eq. (43).

For $u \geq 0$,

- $E_\beta = \Omega^2 - \omega_\beta^2 + 2\lambda_\beta^2$, $G_\beta = E_\beta^2 - 4\lambda_\beta^2 W_\beta$, $\Theta_\beta = E_\beta^2 + 4\lambda_\beta^2 W_\beta$, $\tilde{H}_\beta = 4E_\beta\lambda_\beta$,
- $P_\beta = \omega_\alpha^2 - \omega_\beta^2 + 2\lambda_\beta^2 + 2\lambda_\alpha\lambda_\beta$, $\tilde{Q}_\beta = 2\left(\lambda_\alpha + \lambda_\beta\right)$,
- $U_\beta = G_\beta P_\beta - \tilde{H}_\beta\tilde{Q}_\beta W_\beta$, $\tilde{V}_\beta = G_\beta\tilde{Q}_\beta + \tilde{H}_\beta P_\beta$,
- $R_\beta = k_t^2 + c_t^2\left(\omega_\beta^2 - 2\lambda_\beta^2\right)$, $\tilde{I}_\beta = -2c_t^2\lambda_\beta$,
- $X_\beta = R_\beta U_\beta + \tilde{I}_\beta\tilde{V}_\beta W_\beta$, $\tilde{Y}_\beta = \tilde{I}_\beta U_\beta - R_\beta\tilde{V}_\beta$.

For $u < 0$,

- $E_\alpha = \Omega^2 - \omega_\alpha^2 + 2\lambda_\alpha^2$, $G_\alpha = E_\alpha^2 - 4\lambda_\alpha^2 W_\alpha$, $\Theta_\alpha = E_\alpha^2 + 4\lambda_\alpha^2 W_\alpha$, $\tilde{H}_\alpha = 4E_\alpha\lambda_\alpha$,
- $P_\alpha = \omega_\beta^2 - \omega_\alpha^2 + 2\lambda_\alpha^2 + 2\lambda_\alpha\lambda_\beta$, $\tilde{Q}_\alpha = 2\left(\lambda_\alpha + \lambda_\beta\right)$,
- $U_\alpha = G_\alpha P_\alpha - \tilde{H}_\alpha\tilde{Q}_\alpha W_\alpha$, $\tilde{V}_\alpha = G_\alpha\tilde{Q}_\alpha + \tilde{H}_\alpha P_\alpha$,
- $R_\alpha = k_t^2 + c_t^2(\omega_\alpha^2 + 2\lambda_\alpha^2)$, $\tilde{I}_\alpha = 2c_t^2\lambda_\alpha$,
- $X_\alpha = R_\alpha U_\alpha - \tilde{I}_\alpha\tilde{V}_\alpha W_\alpha$, $\tilde{Y}_\alpha = \tilde{I}_\alpha U_\alpha + R_\alpha\tilde{V}_\alpha$.

where

$$I_\Omega(u) = -\frac{\pi(k_t^2 + c_t^2\Omega^2)}{\Omega^2\Theta_\Omega}\left[\Gamma_I(u)cos(\Omega u) - \Gamma_R(u)sin(\Omega u)\right], \qquad u < 0 \tag{A.6}$$

with

- $\Gamma_R(u) = K_R L_R + K_I L_I(u)$, $\Gamma_I(u) = K_R L_I(u) - K_I L_R$, $\Theta_\Omega = m_\alpha m_\beta$
- $m_\beta = A_\beta^2 + B_\beta^2$; $m_\alpha = A_\alpha^2 + B_\alpha^2$; $K_R = A_\alpha A_\beta + B_\alpha B_\beta$; $K_I = A_\beta B_\alpha - A_\alpha B_\beta$

- $L_R = \frac{2c_t^2\Omega}{k_t^2+c_t^2\Omega^2} - \frac{1}{\Omega} + \frac{2(\Omega A_\alpha - \lambda_\alpha B_\alpha)}{m_\alpha} + \frac{2(\Omega A_\beta - \lambda_\beta B_\beta)}{m_\beta}$;
- $L_I(u) = -u - \frac{2(\Omega B_\alpha + \lambda_\alpha A_\alpha)}{m_\alpha} + \frac{2(\Omega B_\beta + \lambda_\beta A_\beta)}{m_\beta}$
- $A_\alpha = \omega_\alpha^2 - \Omega^2$; $B_\alpha = 2\lambda_\alpha\Omega$; ; $A_\beta = \omega_\beta^2 - \Omega^2$; $B_\beta = 2\lambda_\beta\Omega$;

The integral of I_1 can be derived from I_2 by setting $\alpha = \beta$. We therefore obtain:

$$I_1(u) = \begin{cases} I_{mod}(u), & u \geq 0, \\ I_{mod}(u) + I_\Omega(u), & u < 0. \end{cases} \quad \text{(A.7)}$$

with

$$I_{\text{mod}}(u) = \frac{\pi\, e^{-\lambda_\alpha|u|}}{2\lambda_\alpha\omega_\alpha^2\Theta^2}\left[\left(\lambda_\alpha A + W_\alpha\tilde{B}\right)S_{W_\alpha}(|u|) + \left(A - \lambda_\alpha\tilde{B}\right)C_{W_\alpha}(|u|)\right], \quad \text{(A.8)}$$

and

$$I_\Omega(u) = \frac{\pi(k_t^2 + c_t^2\Omega^2)}{\Omega^2 m_\alpha}[u\cos(\Omega u) + L_R\sin(\Omega u)], \qquad u<0 \quad \text{(A.9)}$$

where

- $R = k_t^2 + c_t^2(\omega_\alpha^2 - 2\lambda_\alpha^2)$, $E = \Omega^2 - \omega_\alpha^2 + 2\lambda_\alpha^2$,
- $G = E^2 - 4\lambda_\alpha^2 W_\alpha$, $\Theta = E^2 + 4\lambda_\alpha^2 W_\alpha$,
- $A = RG - 8c_t^2\lambda_\alpha^2 E W_\alpha$, $\tilde{B} = -2\lambda_\alpha(c_t^2 G + 2RE)$,
- $L_R = \frac{2c_t^2\Omega}{k_t^2+c_t^2\Omega^2} - \frac{1}{\Omega} + \frac{4(\Omega A_\alpha - \lambda_\alpha B_\alpha)}{m_\alpha}$.

Author contributions: CRediT

Gildas Yaovi Amouzou: Conceptualization, Investigation, Methodology, Supervision, Validation, Writing – original draft, Writing – review and editing; **Emile Danho:** Conceptualization, Investigation, Methodology, Supervision, Validation, Writing – original draft, Writing – review and editing. **Isaac Elishakoff:** Conceptualization, Investigation, Methodology, Supervision, Validation, Review and Editing; **Lassiné Keita:** Investigation, Methodology, Validation, Review and Editing.

References

1. Danho E, Amouzou GY. 2015 A dynamic study of a vehicle and prediction of its vertical acceleration on passing through a hump. *Far East Journal of Applied Mathematics* **92**(3), 203–229.
2. Gao W, Zhang N, Dai J. 2008 A stochastic quarter-car model for dynamic analysis of vehicles with uncertain parameters. *Vehicle System Dynamics* **46**(12), 1159–1169.
3. Jiang C, Liu L, Li J, Ni B. 2019 Non-random vibration analysis for general viscous damping systems. *Chinese Journal of Aeronautics* **32**(12), 2655–2666.
4. Long XY, Jiang C, Han X. 2015 New method for eigenvector-sensitivity analysis with repeated eigenvalues and eigenvalue derivatives. *AIAA Journal* **53**(5), 1226–1235.
5. Elishakoff I. 2020 Random vibration of a vehicle model. In *Dramatic effect of cross-correlations in random vibrations of discrete systems, beams, plates, and shells*, pp. 51–62. Cham, Switzerland: Springer International Publishing.

6. Lubliner E, Elishakoff I. 1986 Random vibration of system with finitely many degrees of freedom and several coalescent natural frequencies. *International Journal of Engineering Science* **24**(4), 461–470.
7. Long XY, Elishakoff I, Jiang C, Han X, Hashemi J. 2014 Notes on random vibration of a vehicle model and other discrete systems possessing repeated natural frequencies. *Archive of Applied Mechanics* **84**(8), 1091–1101.
8. Crandall SH, Mark WD. 1963 *Random vibration in mechanical systems*. New York, NY: Academic Press.
9. Lin YK. 1967 *Probabilistic theory of structural dynamics*. New York, NY: McGraw-Hill.
10. Newland DE. 1993 *An introduction to random vibrations, spectral and wavelet analysis*, 3rd edn. London, UK: Longman.
11. Dodds CJ, Robson JD. 1973 The description of road surface roughness. *Journal of Sound and Vibration* **31**(2), 175–183.
12. Robson JD. 1979 Road surface description and vehicle response. *International Journal of Vehicle Design* **1**(1), 25–35.
13. Mikhlin Y, Larin O, Timchenko G, Surhanova Y, Fedotov D. 2026 Forced vibrations of the vehicle with two-level suspension. In Nonlinear Vibrations of Engineering Structures and Their Absorption, pp. 227–253. Cham, Switzerland: Springer Nature Switzerland.
14. Ciocan A. 2005 *Contribution a l'analyse et a la commande du vehicule automobile*. PhD thesis, Université de Picardie, France (in French).
15. Yun S, Lee J, Jang W, Kim D, Choi M. 2023 Dynamic modeling and analysis of a driving passenger vehicle. *Applied Sciences* **13**(10), 5903.
16. Ata WG, Oyadiji SO. 2014 An investigation into the effect of suspension configurations on the performance of tracked vehicles traversing bump terrains. *Vehicle System Dynamics* **52**(7), 969–991.
17. Davis BR, Thompson AG. 2001 Power spectral density of road profiles. *Vehicle System Dynamics* **35**(6), 409–415.
18. ISO 8608. 1995 *Mechanical vibration – Road surface profiles – Reporting of measured data*. Geneva, Switzerland: International Organization for Standardization.
19. Bouazara M. 1997 *Étude et analyse de la suspension active et semi active des véhicules routiers*. PhD thesis, Université Laval, Québec, Canada (in French).
20. Kropáč O, Múčka P. 2008 Effect of obstacles on roads with different waviness values on the vehicle response. *Vehicle System Dynamics* **46**(3), 155–178.
21. Salau TAO, Adeyefa AO, Oke SA. 2004 Vehicle speed control using road bumps. *Transport* **19**(3), 130–136.
22. Sekulić D, Dedović V, Rusov S. 2012 Effect of shock vibrations due to speed control humps to the health of city bus drivers. *Scientific Research and Essays* **7**(5), 573–585.
23. Lombaert G, Degrande G, Clouteau D. 2000 Numerical modelling of free field traffic-induced vibrations. *Soil Dynamics and Earthquake Engineering* **19**(7), 473–488.
24. Garcia-Pozuelo D, Gauchia A, Olmeda E, Diaz V. 2014 Bump modeling and vehicle vertical dynamics prediction. *Advances in Mechanical Engineering* **6**, 736576.
25. Mohammadzadeh A, Haidar S. 2009 On the analysis and design of vehicle suspension systems going over speed bumps. In *2009 ASEE Annual Conference & Exposition*, pp. 14.929.1–14.929.13.
26. Danho E, Amouzou GY, Djué NR, Zokagoa JM, Yanga KKS, Coulibaly N. 2013 Dynamic behavior of a vehicle on a pavement with series of speed bumps type checks. *Far East Journal of Applied Mathematics* **82**(2), 101–122.
27. Pesterev AV, Bergman LA, Tan CA. 2002 Pothole-induced contact forces in a simple vehicle model. *Journal of Sound and Vibration* **256**(3), 565–572.
28. Amouzou GY. 2015 *Dynamique d'un véhicule sur une chaussée pourvue d'aspérités locales*. PhD thesis, Université Félix Houphouët-Boigny (in French).
29. Zuo L, Nayfeh SA. 2003 Structured H2 optimization of vehicle suspensions based on multi-wheel models. *Vehicle System Dynamics* **40**(5), 351–371.

30. Kim H, Yoon YS. 1995 Semi-active suspension with preview using a frequency-shaped performance index. *Vehicle System Dynamics* **24**(10), 759–780.
31. Cong S, Shangbin S. 2015 Vehicle roll stability analysis considering lateral-load transfer rate. In *2015 International Conference on Transportation Information and Safety (ICTIS)*, pp. 398–402. IEEE.
32. Allemang RJ. 2003 The modal assurance criterion – twenty years of use and abuse. *Sound and Vibration* **37**(8), 14–23.
33. Brandt A. 2023 *Noise and vibration analysis: signal analysis and experimental procedures*, 2nd edn. (doi:10.1002/9780470978160)
34. Shin K, Hammond JK. 2008 *Fundamentals of signal processing for sound and vibration engineers*. Chichester, UK: Wiley, 416 pp.
35. Zhang, Y., Sui, G., Jin, X., & Zhang, Y. (2025). Efficient fatigue life assessment strategy via generalizing the Lyapunov equation method by Hilbert transform. Computers & Structures, 314, 107759.